Available online at www.sciencedirect.com
SCIENCE DIRECT®
International Journal of Mass Spectrometry 243 (2005) 1–29
International Journal of Mass Spectrometry
www.elsevier.com/locate/ijms

Review

Gas-phase kinetics and catalytic reactions of small silver and gold clusters

Thorsten M. Bernhardt*

Institut für Experimentalphysik, Freie Universität Berlin, Arnimallee 14, 14195 Berlin, Germany

Received 1 November 2004; accepted 13 December 2004
Available online 15 January 2005

Abstract

Recent work on the chemical reactivity of mass-selected small silver and gold, as well as binary silver–gold cluster ions in a temperature controlled radio frequency ion trap arrangement is reviewed. Reactions with molecular oxygen, carbon monoxide, and mixtures of both reactant gases are investigated, in order to reveal the possible role of these small noble metal cluster ions to act as gas-phase catalysts in the carbon monoxide combustion reaction. The obtained gas-phase reaction kinetics enable the determination of the reaction mechanisms as well as the energetics along the reaction pathway. A strong dependence of the chemical reactivity on cluster size, composition and charge state is found and correlations between electronic structure and reactivity are discussed in terms of simple frontier orbital pictures. Special emphasis is put on the importance of cooperative adsorption effects on the small noble metal clusters. Through comparison of the kinetic data with first principles quantum chemical simulations, a comprehensive picture of the molecular details of the reaction behavior emerges. In particular, the experiments provide evidence that selected cluster ions act as active gas-phase catalysts for the oxidation of CO to CO_2 by molecular oxygen. In the case of Au_2^-, the combination of reaction kinetics measurements with ab initio calculations even revealed the full and detailed reaction cycle of the catalytic gas-phase oxidation of CO.

Keywords: Clusters; Gold; Silver; Ion trap; Reaction kinetics; Catalysis

Contents

* Tel.: +49 30 838 56122; fax: +49 30 838 55567.
E-mail address: tbernhar@physik.fu-berlin.de.

1387-3806/$ – see front matter © 2004 Elsevier B.V. All rights reserved.
doi:10.1016/j.ijms.2004.12.015

1. Introduction

Chemical reactions of gas-phase metal clusters are a very active field of research since the advent of intense cluster sources about two decades ago [1–3]. The fascination for metals in the cluster state of matter originates from the fact that the physical and chemical properties often change over orders of magnitude by the mere addition or removal of one single atom. Thus, the cluster properties are intermediate between the atom and the extended bulk metal, but they cannot simply be scaled down from the macroscopic metal characteristics [4,5]. Moreover, in this non-scalable regime, below about 100 atoms per particle, unanticipated physical and chemical properties of these many body systems might emerge which lead to completely new phenomena [5].

A very prominent recent example in this respect is the catalytic activity of highly dispersed supported gold particles and clusters. Nanometer size gold particles on metal oxide supports efficiently oxidize, e.g., carbon monoxide even at low temperatures, where the activity of common catalyst materials is marginal [6,7]. Since gold is known as noble, hence inert material [8], this counterintuitive observation fostered numerous experimental and theoretical investigations on the chemical reactivity of small gold particles and clusters. Most strikingly, in the non-scalable cluster size regime, mass-selected gold clusters on magnesia with eight atoms actively facilitate the oxidation of CO whereas seven atom gold clusters are completely inert [9]. The reason for this strong size dependence and the mechanism of the oxidation reaction is still unresolved. As one important factor for the catalytic activity, the charge state of the atomic gold clusters was identified in these investigations. Electron transfer from surface defect centers to the cluster-adsorbate complex has been found to be essential to activate catalytic properties [9]. These findings are corroborated by gas-phase reactivity investigations with mass-selected noble metal cluster ions as will be discussed in the next section.

Free charged gold clusters, therefore, seem ideally suited to model key features of heterogeneous gold CO oxidation catalysts, in order to reveal details of the hitherto widely unknown catalytic reaction mechanism and to uncover the influence of charge state and cluster size on the catalytic activity. Furthermore, free gas-phase clusters are experimentally well-defined systems and information on structural and electronic properties are readily available (see below). In addition, due to the finite size of clusters, a direct treatment by first principles simulations is possible and can support the quest for the

origin of catalytic activity and detailed insight into reaction mechanisms.

The same holds for the small clusters of silver. However, nothing is known so far about the capabilities of atomic silver clusters to act as oxidation catalysts. Supported silver catalysts with micrometer particle size are employed commercially in large scale in the important ethylene oxidation processes involving molecular oxygen [10,11]. But although a great deal of information about the catalytic activity of silver is available, the details of the oxidation reaction mechanism remain elusive. Apparently, the rate-determining step involves some form of oxygen bound to the silver particle surface [11,12]. The study of the interaction of silver particles and clusters with molecular oxygen, therefore, might aim to add to an understanding of elementary catalytic reaction steps. In this case again, the experimental techniques of modern cluster science provide two major advantages: first, the reaction system, i.e., the number of atoms in the cluster and the charge state, can be defined exactly in a controlled environment. Second, due to the finite size of clusters a direct treatment by ab initio theoretical approaches is amenable.

The investigations on the reactivity of gold, silver, and also binary silver–gold cluster ions reviewed in the present contribution on one hand demonstrate the unique and unanticipated chemical properties of small noble metal clusters, on the other hand they also might contribute to a possible comprehension of catalytic reaction processes on cluster-like active centers of noble metal catalysts in general. In this respect, the work presented provides some innovations from the experimental point of view: (i) the experimental setup enables controlled temperature dependent gas-phase kinetics measurements of metal cluster reactions which helps to identify reaction mechanisms and energetics; (ii) the employed radio frequency (rf)-ion trap is operated as a reactor for catalysis with trapped mass-selected small metal clusters, and thus permits for the first time the determination of turn-over-frequencies (TOF) of catalytic metal cluster reactions in the gas-phase.

One particular focus of this review will be on the identification of general concepts for cluster reactivity such as, e.g., the cooperative adsorption effects on small metal clusters. Furthermore, it will be demonstrated that the catalytic properties of silver and in particular of gold clusters are very closely related to the size and charge state dependent electronic structures, meaning that indeed each atom (and each electron) counts for the chemical functionality.

To probe the catalytic activity of the small noble metal clusters, the carbon monoxide combustion is employed as a model-type catalytic reaction. Kinetic measurements are also performed on the reactions of the clusters with the reactant gases CO and O_2 separately. In the following sections of this introduction, first the results obtained by other groups on the reactivity of mass-selected free gold and silver cluster ions toward these reactant molecules are briefly reviewed. Subsequently, the CO oxidation reaction itself is discussed and finally the few examples of catalysis by free metal cluster ions already known in the literature are presented.

1.1. Chemical properties of free mass-selected silver and gold clusters

Positively charged gold clusters in the size range with up to about 20 atoms per cluster are essentially unreactive toward molecular oxygen [13–15]. The same result was found for neutral gold clusters. In contrast, gold cluster anions show a pronounced odd–even alternation with cluster size in their reactivity toward O_2. This remarkable size and charge state dependence of the reactivity of free gold clusters toward small molecules was first recognized more than a decade ago [13,16] and confirmed by several other groups later on [17,18]. Fig. 1a presents a compilation of the results on Au_n^- reactivity toward O_2. Since gold is an s^1 valence electron metal, its physical properties such as, e.g., ionization potential [19] and electron affinity [20–22] also alternate with cluster size in the small size regime. The close relation of gold cluster electron affinity and reactivity toward molecular oxygen has been discussed by several groups [13,17,18,23]. The reactions of gold cluster ions, positively as well as negatively charged, with carbon monoxide have also been reported [17,24–27]. However, although strong size effects in reactivity are apparent, no odd–even alternations are observed in this case as can be seen for Au_n^- from Fig. 1b, which is based on the results of Lee and Ervin [17] as well as of Wallace and Whetten [27].

The physical properties of small silver clusters have been explored in great detail experimentally and theoretically [20,21,28–32] and have been found to be as well dominated by their s^1 valence electron structure, as expected. Fig. 1c shows the reactivity of negatively charged silver clusters toward O_2 [17,33], which resembles the Au_n^- reactivity in the sense that it also alternates in an odd–even fashion with cluster size. However, the small gold cluster anions only adsorb one or none oxygen molecule depending on cluster size, whereas anionic silver clusters are able to adsorb more than one O_2, due to strong cooperative effects as will be discussed in detail below [33]. The reactions of neutral and positively charged silver clusters with oxygen have also been investigated previously. Interestingly, the neutral clusters are again unreactive toward molecular oxygen [34,35]. Ag_n^+, in contrast, show temperature dependent molecular and dissociative adsorption of oxygen [36–39], demonstrating already the propensity of silver clusters to activate the oxygen molecular bond. Whereas negatively charged silver clusters have been reported to be unreactive toward carbon monoxide [17,40], nothing is known so far about the reactions of silver cluster cations with carbon monoxide.

1.2. Carbon monoxide combustion reaction

The oxidation of carbon monoxide by molecular oxygen is considered a model surface reaction in heterogeneous catal-

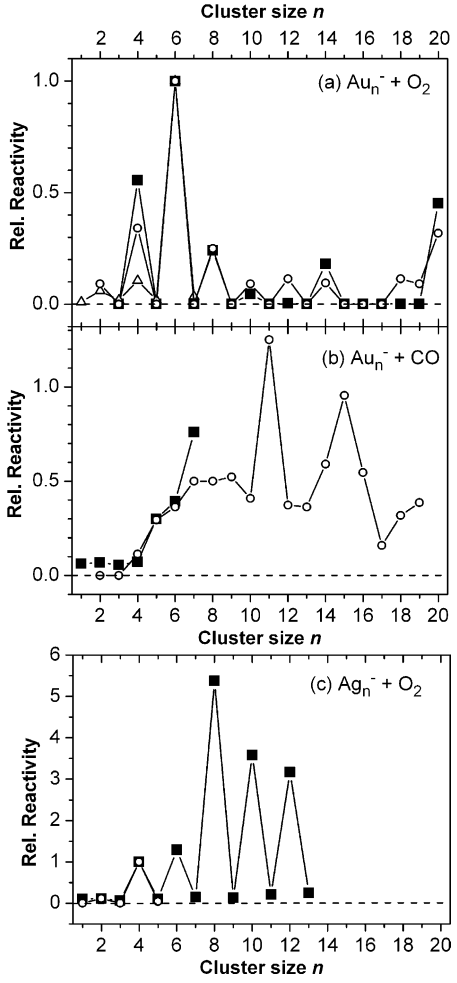

Fig. 1. Compilation of experimental results from the literature on the relative reactivity of gold and silver cluster anions in the adsorption reaction of one O_2 or one CO molecule, respectively, as a function of the cluster size n. (a) Reactions of Au_n^- with O_2: (■) data from Ref. [13], (Δ) data from Ref. [17], (◯) data from Ref. [18]. For comparison, all data are normalized to the reactivity of Au_6^-. (b) Reactions of Au_n^- with CO: (■) data from Ref. [17], (◯) data from Ref. [27]. Again, the data shown have been normalized to the reactivity of Au_6^- toward O_2. (c) Reactions of Ag_n^- with O_2: (■) data from Ref. [17], (◯) data from Ref. [33]. For comparison, in this case, all data are normalized to the reactivity of Ag_4^-.

ysis [41,42]. It is also of great practical importance, e.g., in automotive exhaust decontamination [41]. In the present context, this reaction will be employed to probe the catalytic activity of mass-selected noble metal cluster ions. The CO combustion reaction:

$$2CO + O_2 \rightarrow 2CO_2,$$

although exothermic by 283 kJ mol^{-1} [43], does not proceed in the gas-phase under ambient conditions due to a high activation energy barrier, which mainly results from the necessity to break the oxygen molecular bond. Thus, the activation or cleavage of the O–O bond is the major step to facilitate the reaction. This is readily achieved by transition metal catalysts, in particular by the platinum-group metals [41]. The reaction on the metal catalyst surface proceeds via

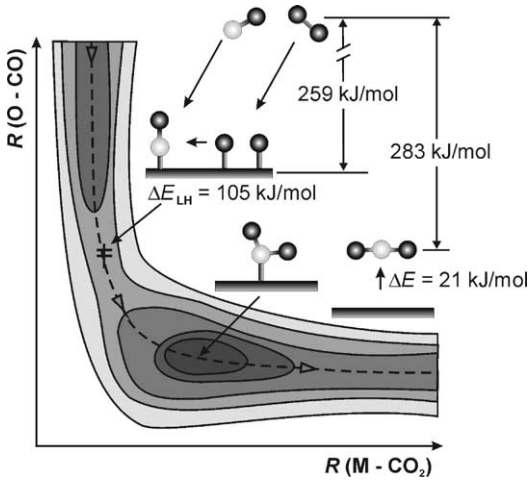

Fig. 2. Two-dimensional potential energy diagram of the CO oxidation reaction on a platinum(1 1 1) surface with the involved energies indicated (dark shaded area correspond to potential energy minima; see also text). The mutual O—CO distance of the unreacted system R(O—CO) is plotted vs. the CO_2—Pt distance R(M—CO_2). The reaction proceeds (at low coverages) via a Langmuir–Hinshelwood mechanism. The reaction coordinate is marked by the dashed line (adapted from refs. [41,45]). The light spheres represent carbon atoms, dark spheres oxygen atoms.

a Langmuir–Hinshelwood (LH)-type mechanism [41], i.e., CO and O are first adsorbed on the surface, whereby the spontaneous dissociation of the diatomic oxygen molecule is presumed. The reactants subsequently diffuse on the surface before forming a reactive surface complex, which leads to the CO_2 formation. Coadsorption studies reveal that repulsive interactions due to the necessity of electronic charge restructuring around the surface complex dominate the encounter between neighboring adsorbed CO and O particles [44] and lead to a reaction-activation barrier. Furthermore, the shape of the product (CO_2) molecule usually differs from the shape of the surface intermediate, i.e., the transition state or activated complex, which is assumed to be bent in this case. The respective reorientation of molecular orbitals (MO) will also contribute to an activation energy barrier.

Fig. 2 presents a two dimensional representation of the potential energy surface, where the adsorption bond length for the CO_2 product molecule is plotted on the x-axis and the mutual distance R(O–CO) between the adsorbed reactants O_{ad} and CO_{ad} is plotted on the y-axis. The graphic is based on the report by Ertl on CO oxidation on a platinum (1 1 1) surface [45]. All energies are referred to the gaseous reactants ($CO + (1/2)O_2$) in molar concentrations. Starting from the upper left, the adsorption of one mol of CO and O is accompanied by a net energy gain of 259 kJ. Adsorbed O and CO resides in the deep potential energy minimum on the upper left side of the diagram. As the reaction proceeds, both species must move up-hill along the dashed line to reach the transition state (denoted by the symbol ‡), before CO_2 can actually be formed. This passage requires the aforementioned activation energy ΔE_{LH} of about 100 kJ. The CO_2-surface complex is very weakly adsorbed in a shallow

potential well from which it can easily escape and leave the surface (adsorption energy of ∼20 kJ mol^{-1}). The gaseous CO_2 then exhibits the well-known thermodynamic reaction enthalpy of 283 kJ mol^{-1} as compared to the reactants. For the case of free gold clusters, it has been discussed theoretically, whether the CO oxidation reaction might proceed via the surface analogous Langmuir–Hinshelwood mechanism, involving adsorbate diffusion on the clusters [8,27], or via an Eley–Rideal (ER)-type mechanism, in which the reactant has to collide at the right position with the cluster-complex to initiate the reaction [41,46]. The gas-phase kinetics measurements in combination with theoretical results presented in the present review will provide evidence to resolve this issue.

As discussed, in general atomic oxygen is the reaction partner of CO on transition metal surfaces. However, with a scanning tunneling microscope, on a Ag(1 1 1) surface, tip induced CO oxidation with molecularly adsorbed oxygen at low temperatures has been achieved [47]. In these experiments, intermediate COO_2-complexes could be identified by tunneling spectroscopy. This kind of intermediate resembles the complexes of the same stoichiometry that have been observed by infrared spectroscopy when gold atoms are condensed into a matrix consisting of O_2 and CO at cryogenic temperatures. In these matrix systems, even gold atom induced CO_2 formation could be identified, when the matrices were warmed up to 40 K [48]. Therefore, another key question of gas-phase metal cluster CO oxidation is, whether molecularly or atomically adsorbed oxygen is required for the catalytic CO_2 formation. In this regard, recent high resolution photoelectron spectroscopy experiments on anionic gold and silver clusters with adsorbed O_2 provide valuable evidence that the dioxygen remains molecularly bound on the gold clusters Au_n^- with even n up to $n = 20$ [49–52] as well as on the small silver clusters Ag_n^- with even n up to $n = 14$ [53]. From the vibrationally resolved photoelectron spectra, an O–O bond elongation due to electron charge transfer from the metal cluster anion to the oxygen molecule has been deduced [51].

1.3. Catalysis with free metal clusters

Several gas-phase catalytic processes promoted by free atomic metal ions have been reported [54] and two very recent reviews provide an excellent overview over this subject [55]. The first investigations on the catalytic activity of metal cluster ions have been carried out in an ion cyclotron resonance mass spectrometer by Irion and co-workers [56]. They demonstrated the conversion of ethylene to benzene by Fe_4^+ cluster cations. However, the removal of the benzene in the final reaction step to recover the initial Fe_4^+ cluster was only achieved by collision-induced dissociation with at least 3.2 eV collision energy.

A catalytic metal cluster ion reaction cycle under thermal conditions was observed by Ervin and co-workers. This group demonstrated that gas-phase platinum cluster anions, Pt_n^- ($n = 3$–7), efficiently catalyze the oxidation of CO to CO_2 by N_2O or O_2 near room temperature in a combined flow tube and gas cell reactor instrument [57]. As intermediate products of the catalytic reaction $Pt_nO_2^-$ and in particular Pt_nO^- ions were detected which provides evidence that in this case O_2 seems to be rather dissociatively adsorbed on the metal cluster as oxygen atoms, than chemisorbed or physisorbed as molecular O_2. In further work of this group, the activity of palladium cluster anions in the CO oxidation catalysis was examined and it was found that Pd_n^- also efficiently catalyzes the CO combustion reaction [3].

Although these two examples presented by the group of Ervin were the only thermal catalytic reaction cycles of free metal clusters observed so far, and although only the completion of a single reaction cycle could be detected in the experiments, the prospects of free metal cluster catalysis studies appear promising. In particular, the possibility to gain insight into reaction mechanisms under controlled conditions, to study the influence of cluster size, and eventually to approach the bulk limit are definitely appealing. Interestingly, parallel to our investigations, Ervin even suggested recently to employ an ion trap as catalytic reactor for gas-phase metal cluster ion catalysis studies or applications, respectively, [3]: *It is an interesting exercise to consider the possible practical use of gas-phase metal cluster catalysis. One could, in principle, design an ion trap reactor in which the metal cluster ions are held and through which CO and O_2 reactants flow*. Our experimental realization of this concept and its use for reaction kinetics studies as well as the discovery and analysis of noble metal cluster catalytic reactions will be discussed in the following sections.

2. Experimental

The guided ion beam technique employed in the present investigation is a well-established method in gas-phase cluster chemistry [2,28,58]. The instrument comprises cluster generation by sputtering of metal targets and mass-selection as well as ion guidance via quadrupole techniques. Our experimental approach to investigate metal cluster reactions consists in storing the mass-selected cluster ions in a temperature variable rf-octopole ion trap filled with helium buffer gas and small partial pressures of reactant gases. The major advantages of this approach are the precise control over reaction time, reactant concentrations, and reaction temperature inside the ion trap. The trap thus acts like a test tube for gas-phase reaction kinetics studies.

2.1. rf-ion trap apparatus

The schematic layout of the experimental setup consisting of the rf-octopole ion trap inserted into a multiple quadrupole mass spectrometer arrangement is displayed in Fig. 3. Metal clusters are prepared by simultaneous sputtering of four metal targets with accelerated xenon ion beams of 12 keV kinetic

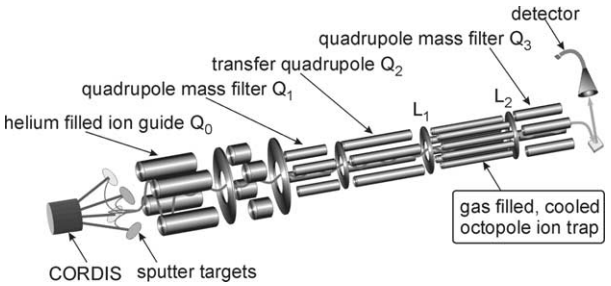

Fig. 3. Experimental setup for the investigation of reaction kinetics and catalytic activity of free mass-selected metal clusters. The cluster ions are sputtered from solid targets with a cold reflex discharge ion source (CORDIS), mass-selected (Q_1), and guided at low energies (Q_0 and Q_2) into the temperature controllable octopole ion trap. By means of appropriate switching of the lenses L_1 and L_2, the reaction products are extracted and subsequently mass analyzed by another quadrupole mass filter (Q_3).

energy. The xenon ion beams are generated by a cold reflex discharge ion source (CORDIS) [59] and directed onto the targets by an electrostatic lens system. The charged clusters sputtered from the targets are steered into the first helium filled quadrupole Q_0 (cf. Fig. 3), which serves to collimate and thermalize the cluster ions. The ion beam is further guided into a mass-selective quadrupole filter Q_1 to record and to optimize the cluster ion distribution prepared by the sputter source and to select one particular clusters size. Mass spectra of negative cluster ion distributions obtained for different target materials (silver, gold, or silver–gold alloy) are shown in Fig. 4. The ion intensities in these experiments have been optimized for the small cluster size regime.

Subsequently, the cluster ions are transferred with a third quadrupole Q_2 into the home-built octopole ion trap [36,60]. Inside Q_2, the cluster beam is again thermalized by collisions with helium buffer gas prior to entering the ion trap. The potential on the entrance lens L_1 of the ion trap is chosen just below the kinetic energy of the ion beam so that the cluster ions are able to enter the trap (see Fig. 3). They traverse the trap (80 mm length) and are reflected by the repulsive potential on the back electrode (exit lens L_2) of the trap. A simulated trajectory of an Au_2^- cluster ion inside the octopole ion trap at thermal kinetic energy (25 meV) is shown in Fig. 5a. This ion path was calculated without considering collisions with the buffer gas [61]. However, during the experiments the octopole ion trap is pre-filled with about 1 Pa partial pressure of helium buffer gas. Thus, the cluster ions experience frequent collisions with the buffer gas (the collision frequency in our experiment is about $3 \times 10^5\ s^{-1}$). Fig. 5b shows an enlarged view of a cluster ion trajectory propagating during a time window of 300 μs. On this excerpt of the ideal trajectory, the cluster ion would experience about 100 collisions with the buffer gas, each of which would change the propagation direction and velocity of the cluster ion.

The ion trap assembly is attached to a helium cryostat allowing variable temperature adjustment in the range between 20 and 350 K. The buffer gas collisions ensure that thermal equilibration of the clusters entering the trap is achieved

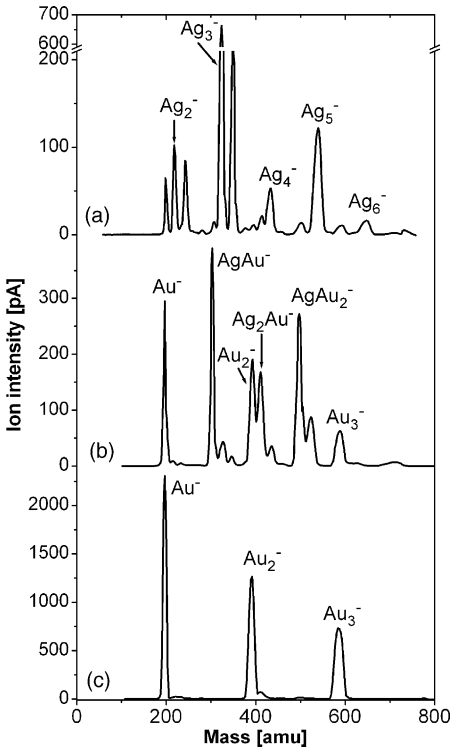

Fig. 4. Cluster anion distributions generated by the CORDIS sputter source from different target materials. The mass spectra were obtained by scanning the mass-selective filter Q_1 (see Fig. 3) and recording the ion currents on the rods of transfer quadrupole Q_2 acting as a Faraday collector. The ion currents were optimized for the small cluster size regime up to 800 amu. Cluster distributions were obtained by using (a) pure silver targets, (b) silver–gold alloy targets with composition Ag 70%: Au 30%, and (c) pure gold targets [70].

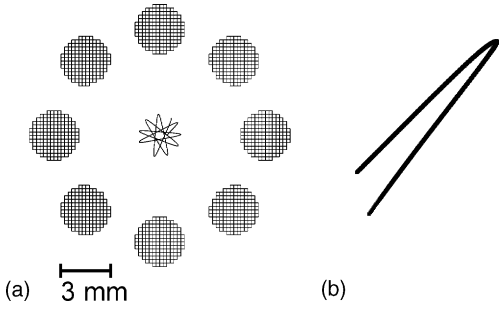

Fig. 5. Ion trajectory simulation inside the octopole ion trap calculated employing the SIMION software [61]. (a) Cross-section view showing the eight rods of the trap and the trajectory of an Au_2^- (394 amu) ion. The ion kinetic energy was chosen to be 25 meV corresponding to room temperature thermal conditions. The ion starting point is 2 mm off center of the trap. The conditions are assumed ideal, i.e., no buffer gas conditions are considered. An rf-frequency of 1.06 MHz at an amplitude of about 100 V is applied to the rods to effectively confine the cluster ion to the center of the trap. (b) Enlarged view of a part of the ion trajectory corresponding to a propagation time of 300 μs. The ion starting point is 1 mm off center of the trap. During this time, the ion would experience about 100 buffer gas atom collisions under our experimental conditions (helium buffer gas density: $2 \times 10^{12}\ mm^{-3}$). Note that each buffer gas collision would change the ion trajectory direction and the ion energy [121].

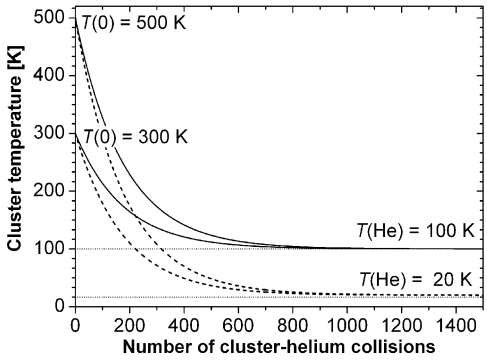

Fig. 6. Thermalization efficiency of trimer cluster ions inside the helium filled coolable octopole ion trap. The graphs are calculated according to Ref. [62]. The cluster temperature is plotted as a function of the number of cluster–helium collisions. The solid graphs represent conditions in which the buffer gas temperature is T(He) = 100 K and the cooling process starts from an initial cluster temperature of T(0) = 500 or 300 K, respectively. The dashed graphs show the evolution starting from the same T(0) values, but approaching a final buffer gas temperature of T(He) = 20 K. In all these cases, thermal equilibration is achieved in less than 1000 buffer gas collisions, which corresponds to less than a millisecond under the experimental conditions.

within less than a few thousand collisions, i.e., in a few milliseconds under our operating conditions. Fig. 6 presents a simulation of the thermalization efficiency according to Ref. [62]. The temperature of a trimer cluster is plotted as a function of the number of cluster–helium collisions. It is apparent from this graph that the cluster assumes the trap temperature T(He) within less than thousand buffer gas collisions, regardless of the initial cluster temperature T(0) (300 or 500 K) and also almost independent of the aspired buffer gas, i.e., ion trap temperature T(He) (20 or 100 K). Also the cluster size has only a minor influence on the thermalization time. A 13-atom cluster, e.g., was simulated to be thermalized within less than 3000 buffer gas collisions [62]. The complete and rapid thermalization of the clusters inside the ion trap and the efficient translational to internal energy transfer was verified by temperature and pressure dependent real-time laser probing of the nuclear cluster dynamics. Variation of the buffer gas pressure between 0.2 and 0.9 Pa had no influence on the strongly temperature dependent time-resolved pump-probe signal that reflects very sensitively the nuclear cluster dynamics [60]. This confirms the complete thermalization of the cluster ions inside the ion trap. Whereas thermalization is thus accomplished within a few milliseconds, the cluster ions are stored in the trap for a considerably longer time period, typically for several seconds, without significant ion loss.

The trap is filled with gold cluster anions up to the space charge limit, i.e., about 10^4 ions per mm^3. This value represents the initial concentration of the metal cluster reactants. In addition to the helium buffer gas, a small well-defined fraction of reactive gases (CO and O_2) is added to the ion trap. The absolute partial pressures inside the trap are measured by a baratron gauge (MKS, Typ 627B). The potentials on the entrance and exit lenses, L_1 and L_2, can be computationally switched in order to fill the trap and store the ions in the trap. After the chosen reaction time, i.e., storage time, all ions, reactants, intermediates, and products, are extracted by applying an electrostatic field, and the ion distribution is analyzed via the final quadrupole mass filter Q_3 (Fig. 3). The ion pulses are amplified by a channeltron/conversion dynode detector and digitalized and integrated by a LeCroy 9400A 175 MHz oscilloscope. By recording all ion concentrations as a function of the reaction time, the kinetics of the reaction may be obtained.

2.2. Kinetic evaluation procedure

The concentrations of the reactive gases in the octopole trap are orders of magnitude larger than the metal cluster ion concentration and, in addition, there is a steady flow of reactants (O_2 and CO) during the reaction. Therefore, the reactant concentrations are considered to remain constant in the kinetic evaluation procedure [63,64]. Hence, all the proposed reaction steps are assumed to follow pseudo first order kinetics. Possible reaction mechanisms are evaluated by fitting the integrated rate equations to the experimental kinetic data. The integration of the rate equations is performed numerically by using the fourth order Runge–Kutta algorithm. The employed fitting procedure consists of an iterative nonlinear least-square method [65]. Our method is the basic approach to macroscopic chemical kinetics [63,64] and results in an optimized kinetic model presenting the most simple reaction mechanism with the best fit to the experimental data. Note that in this approach more complex mechanisms, which result in the same fit quality are discarded. Thus, the obtained reaction steps are not necessarily elementary reaction steps, as will be seen below. Furthermore, Benson's rule of chemical kinetics [63,64] applies to all deduced reaction mechanisms.

In order to demonstrate the kinetic analysis procedure, first, the reactivity of the Au_2^- dimer anion toward molecular oxygen is presented. In agreement with previous studies (see also discussion of Fig. 1), $Au_2O_2^-$ is the only product in this reaction [16–18,25,66]. The product ion signals, normalized on the initial Au_2^- concentration and on the total ion concentration in the trap, as a function of the reaction time t_R are displayed in Fig. 7 for three different temperatures. These kinetics can best be fitted by a straightforward association reaction mechanism:

$$Au_2^- + O_2 \rightarrow Au_2O_2^- \quad (1)$$

The solid lines in Fig. 7 represent the fitted integrated rate equations for this mechanism. An excellent match to the experimental data is observed for all temperatures. The obtained corresponding pseudo first order reaction rate constants k for a series of experiments at various temperatures is listed in Table 1. Most notably, the reaction rate appears to increase with decreasing reaction temperature (cf. also Fig. 7). Considering Arrhenius' classical empirical equation for the

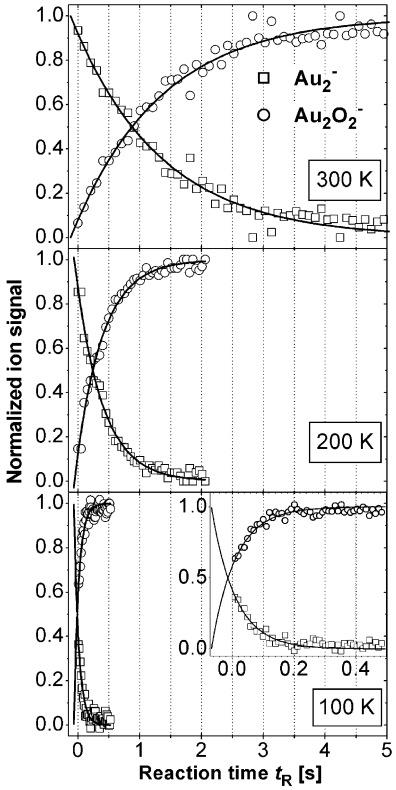

Fig. 7. Temperature dependent kinetics of the reaction of Au_2^- with O_2. The open symbols represent the experimental data. The normalized concentrations of Au_2^- (□) and the reaction product $Au_2O_2^-$ (◯) are plotted as a function of the reaction time t_R for three different reaction temperatures. The solid lines are obtained by fitting the integrated rate equations of the proposed reaction mechanism Eq. (1) to the experimental data. For very fast reactions, the ion trap filling time is relevant for the reaction time. Therefore, in this case, the time zero of the plotted reaction time t_R is slightly shifted, in particular for the 100 K data (cf. inset) [95].

temperature dependence of reaction rates:

$$k(T) = \nu \exp\left(-\frac{E_a}{RT}\right) \tag{2}$$

with k being the rate constant, ν the frequency factor, T the temperature, R the gas constant, and E_a the activation energy of the reaction, the observed inverse dependence of the reaction rate on the temperature would require the inference of a negative activation energy E_a [64]. This is indicative for the prevalence of a more complex elementary reaction scheme, which will be detailed in the following section.

Table 1
Measured pseudo first order and calculated termolecular reaction rate constants for the reaction of Au_2^- with O_2 at different reaction temperatures T

T (K)	p(He) (Pa)	$p(O_2)$ (Pa)	k (s^{-1})	$k^{(3)}$ (10^{-28} cm^6 s^{-1})[a]
100	1.03	0.04	5.52 ± 0.60	8.11 ± 2.03
150	1.05	0.06	2.49 ± 0.35	3.29 ± 0.55
190	1.05	0.08	1.13 ± 0.11	1.54 ± 0.19
200	1.00	0.16	1.38 ± 0.12	1.04 ± 0.10
300	1.05	0.13	0.62 ± 0.03	0.82 ± 0.07

[a] For the calculation of $k^{(3)}$, the measured pressures have been corrected by a thermal transpiration factor [123].

2.3. Low-pressure reaction kinetics

The total pressure inside the ion trap is on the order of 1 Pa which means that the experiment is operating in the kinetic low-pressure regime. Therefore, a Lindemann-type mechanism has to be considered for each reaction step and the reaction rates depend on the buffer gas pressure [63,64]. As a consequence, the obtained pseudo first order rate constant k contains the termolecular rate constant $k^{(3)}$ as well as the concentrations of the helium buffer gas and of the reactants; in the case of reaction (1) (Fig. 7):

$$k = k^{(3)}\,[\mathrm{He}][\mathrm{O_2}]. \tag{3}$$

The termolecular rate constants $k^{(3)}$ calculated accordingly for this reaction are also included in Table 1. They are in complete agreement with the rate constant measured previously by Lee and Ervin for this reaction which amounts to $3.9 \pm 2.6 \times 10^{-28}$ cm^6 s^{-1} [17].

The details of the reaction are described by the Lindemann energy transfer model for association reactions, which is represented by the following equations [63,64,67]:

$$Au_2^- + O_2 \underset{k_d}{\overset{k_a}{\rightleftarrows}} Au_2O_2^{-*} \tag{4a}$$

$$Au_2O_2^{-*} + He \xrightarrow{k_s} Au_2O_2^- + He^*. \tag{4b}$$

The reaction model includes the elementary steps of the initial formation of an energized complex $Au_2O_2^{-*}$ (rate constant k_a) and its possible unimolecular decomposition back to the reactants (k_d) in competition with a stabilizing energy transfer collision with helium buffer gas (k_s). Assuming all these elementary reaction steps to be again of pseudo first order and employing steady-state assumption for the intermediate, the overall third order rate expression is obtained to be [68]

$$k^{(3)} = \frac{k_a k_s}{k_d + k_s[\mathrm{He}]}. \tag{5}$$

As the experiment is operating in the kinetic low pressure regime the decomposition rate constant can consequently be considered to be much larger than the stabilization rate constant term: $k_d \gg k_s[\mathrm{He}]$. This leads to a simplified expression for the termolecular rate constant, which can be applied to the present experimental conditions:

$$k^{(3)} = \frac{k_a k_s}{k_d}. \tag{6}$$

The ion–molecule association rate constant k_a as well as the final stabilization rate constant k_s are well represented by ion–molecule collision rate coefficients as specified by Langevin theory [68]. According to this theory, ion–molecule reactions are basically charge-induced dipole interactions and exhibit no activation barrier, i.e., no temperature dependence

[69]. For the present example, the calculated values amount to $k_a = 5.45 \times 10^{-10}$ and $k_s = 5.26 \times 10^{-10}$ cm^3 s^{-1}, respectively, independent of the reaction temperature. The observed inverse temperarture dependence of $k^{(3)}$ (cf. Table 1), therefore, originates from the activation barrier of the unimolecular decomposition of the metastable intermediate complex $Au_2O_2^{-*}$ back to the reactants (k_d is contained in the denominator of Eq. (6)). In order to estimate k_d, statistical rate theory, such as Rice–Ramsperger–Kassel (RRK)-theory or Rice–Ramsperger–Kassel–Markus (RRKM)-theory may be employed [70,71]. For each reaction step, identified in the kinetic evaluation and fitting procedure, a Lindemann-type reaction scheme as described above has to be considered as elementary reaction scenario.

3. Size dependent electronic structure of silver and gold clusters

The aim of this section is to give a brief overview over the size and composition dependent electronic properties of small silver, gold, and binary silver–gold clusters which will prove to be useful for the later discussion of reactive properties and adsorption kinetics of these clusters. The experimental vertical electron detachment energies (VDEs) of silver, gold, and some silver–gold binary cluster anions with up to 10 atoms per cluster are summarized in Fig. 8. The values in this graph are taken from selected references only [20,21,72,73], for the sake of clarity, but similar data have been reported by other groups [22,30,74,75]. General trends of the electronic structure of silver and gold clusters have already been presented briefly in Section 1.1, but three particular important issues, which are apparent from Fig. 8, will be emphasized here: (i) as mentioned earlier, the odd–even alternation in VDE values with cluster size can be attributed largely to the s^1 valence electron structure of group Ia transition metal elements

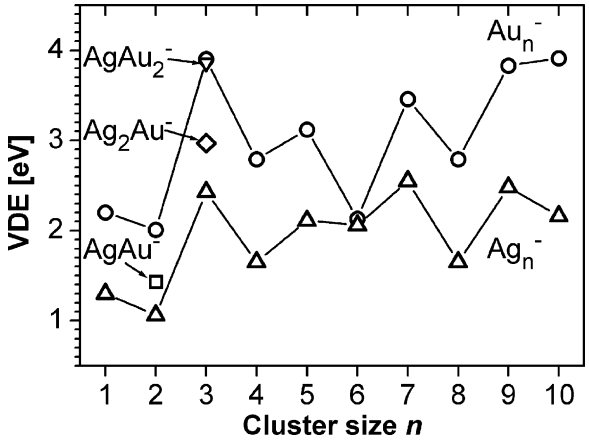

Fig. 8. Compilation of experimental vertical detachment energies (VDEs) from the literature for anionic silver, gold and binary silver–gold clusters as a function of the cluster size n. (△) Ag_n^- VDEs from Ref. [20]; (◯) Au_n^- VDEs from refs. [20,21,72]; VDEs of $AgAu^-$ (□), Ag_2Au^- (◇), and $AgAu_2^-$ (▽) are from Ref. [73].

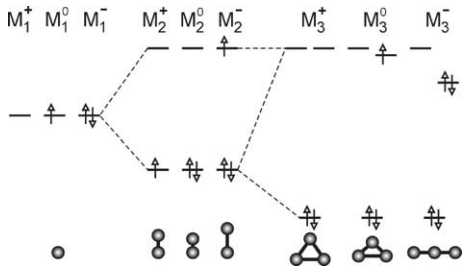

Fig. 9. Schematic representation of the evolution of molecular s orbital energies and electron occupations with cluster size and charge state up to the trimer. Also shown are general geometric structures, which are to be expected for the noble metal dimers and trimers in the different charge states.

silver and gold. Electronic closed shell (paired electron) cluster sizes are generally more stable and exhibit higher VDEs than open shell systems. A schematic representation of the s-level evolution with cluster size and charge state up to the trimer is depicted in Fig. 9. Also included in this figure are the expected general trends in geometrical structure for these small clusters. The dimer anion has the unpaired electron in an anti-bonding orbital resulting in the largest bond distance with respect to the structure in the other charge states. The same (one electron in an anti-bonding orbital) is true for the neutral trimer, which leads in this case to a Jahn–Teller distorted obtuse triangular structure. The anionic noble metal trimers always acquire a linear geometry in the $^1\Sigma_g^+$ electronic ground state. (ii) From Fig. 8, it can also be seen that the VDE values of the gold cluster anions are in general roughly about 1 eV higher than the VDE values of the corresponding silver clusters (with the exception of Au_6^- [72,75,76]). These stronger bonding of the outermost electron in the gold clusters is clearly a consequence of the relativistic effects prominent in gold which lead to a contraction of the s- and p-type electronic orbitals, and thus to a higher binding energy for the corresponding electrons [77]. (iii) The VDE values for the binary silver–gold clusters are somewhat located in between the corresponding silver and gold cluster data. However, Fig. 8 shows that the change in VDE in going from pure silver to pure gold cluster anions is not continuous, as it might be expected, e.g., from the continuous work function change with composition in silver–gold alloys [78]. In particular, the VDE of $AgAu_2^-$ is almost similar to that of Au_3^-, whereas the Ag_2Au^- value is closer to Ag_3^- than to Au_3^-.

It has been discussed by several authors that, although silver and gold belong to the same group in the periodic system and the atomic electronic structure of both exhibit a filled d shell and a singly occupied s shell ($nd^{10}(n+1)s^1$, with $n = 4$ for silver and $n = 5$ for gold), the bonding in gold compounds and clusters is substantially different from that of silver. This phenomenon is referred to as 'gold anomaly' [77,79]. The differences in the physical and chemical properties of silver and gold clusters can be attributed primarily to relativistic effects [77,79–82].

The main relativistic effect in gold is the stabilization of the $6s^1$ orbital and the destabilization of the $5d^{10}$ orbitals, thus

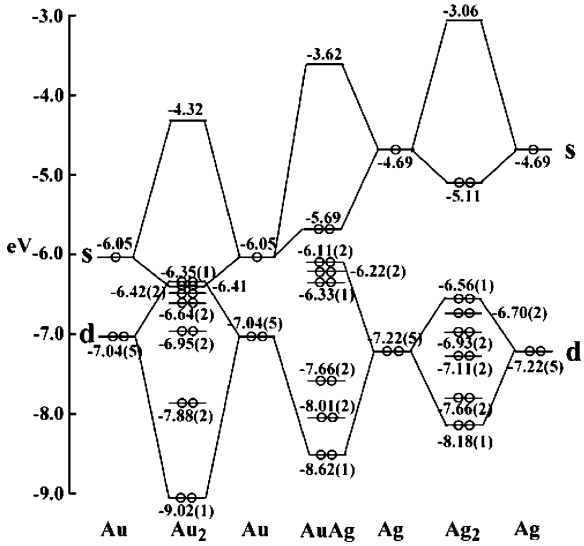

Fig. 10. Molecular orbital (MO) energies of Au_2, AgAu, and Ag_2. The occupied electrons are shown as circles. The value in parentheses are the numbers of degenerate states of the d orbital-type MOs. The figure is taken from Ref. [82].

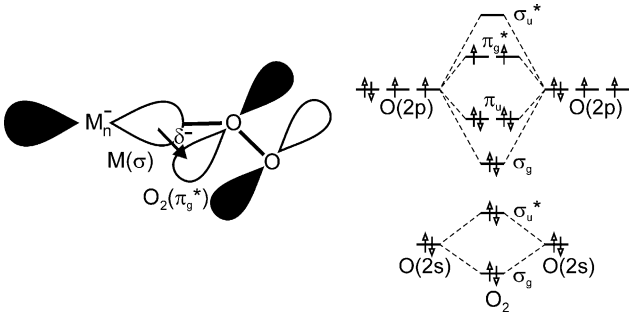

Fig. 11. Left: schematic MO picture of the interaction of molecular oxygen with silver and gold cluster anions M_n^-. O_2 acts as an electron acceptor through the π_g^* anti-bonding orbitals. Electronic charge (δ^-) is transferred out of the highest occupied molecular orbital (HOMO) of the metal cluster anions, which is of σ-type symmetry in the case of silver and gold clusters, into the π_g^* anti-bonding orbitals. Right: schematic MO bonding scheme of O_2 [122].

bringing them energetically closer [81]. The result is a hybridization of atomic s and d states in the case of gold, which has important implications on the chemistry of gold clusters [77,79], as will be seen below, but also on their geometrical structure. Gold cluster anions, e.g., are planar in structure up to a size of about 12 atoms [72,81,83], whereas silver clusters are three-dimensional from Ag_6^- on [31,84]. With respect to the cluster geometry also the charge state plays an important role: neutral gold clusters Au_n are calculated to be planar up to at least $n = 10$ [85], for Au_n^+, however, ion mobility measurements indicate a transition to three-dimensional structures from $n = 8$ on [86]. The differences in the bonding of the dimers Ag_2, AgAu, and Au_2 can be seen from the calculated molecular orbital energies [82] presented in Fig. 10. The silver dimer has a large s–d energy difference, which decreases considerably on going to the mixed dimer and completely vanishes in the case of Au_2. This calculated evolution is also confirmed by in the spectroscopic properties of Au_2 and Ag_2. The excited states of Ag_2 arise from $5s \rightarrow 5p$ excitation, in contrast, the excited states of Au_2 arise from $5d \rightarrow 6s$ promotion. While the first excited state of Au_2 ($^3\Sigma_u^+$) is identical to Ag_2, all other excited states appear in a different order [77].

4. Cluster structure and reactivity

In this section, product ion mass spectra and kinetic measurements of noble metal cluster gas-phase adsorption reactions inside the rf-ion trap will be presented. O_2 and CO adsorption will be investigated separately as a function of cluster charge state, size, and composition, before the results of coadsorption measurements will be presented. The experimental results will be discussed by employing simple frontier orbital considerations and an emphasis will be put on the effects of cooperative adsorption of two reactant molecules onto the trapped cluster ions.

4.1. O_2 adsorption

4.1.1. Frontier orbital model of O_2 adsorption

The degenerate $2p\pi_g^*$ anti-bonding orbitals of oxygen are each occupied by an unpaired electron (cf. MO schema on the right hand side of Fig. 11). This triplet open-shell electronic ground state structure is rather unusual for stable molecules and leads to an electron acceptor behavior similar to the one found in the NO_x family of free radicals [18]. Oxidative addition to the cluster requires interaction of an O_2 π_g^* orbital with the highest occupied molecular orbitals (HOMO) of the noble metal cluster, which has σ-type symmetry. This is schematically depicted in Fig. 11 (left hand side) for the case of negatively charged silver or gold clusters M_n^-. The observed odd–even alternations in reactivity of M_n^- toward O_2 with clusters size (see Fig. 1a and c) can be rationalized qualitatively by considering these frontier orbital interactions: In the case of even n clusters, the M_n^- HOMO has an unpaired electron (cf. Fig. 9) with relatively low binding energy (see VDEs in Fig. 8). In the bound complex $M_nO_2^-$, this electron is easily paired with the single electron in one O_2 π_g^* orbital. The combination of the two orbitals results in an attractive interaction and a partial electron transfer to the O_2 adsorbate (indicated by the symbol δ^{-1} in Fig. 11). In contrast, for odd n clusters, the M_n^- HOMO is doubly occupied (Fig. 9) leading to higher VDEs (Fig. 8). Consequently, the electron transfer to the adsorbate is considerably weaker, meaning that the interaction with the O_2 π_g^* is much less attractive, because the additional electron must be placed in the anti-bonding orbital of the $M_nO_2^-$ complex. As a result, the reactivity of even n silver and gold cluster anions toward molecular oxygen is by far superior to that of odd n clusters [17,18,33,40]. Detailed first principles quantum chemical calculations on the

bonding of molecular oxygen to negatively charged gold and silver clusters [46,52,87–89] but also to positively charged silver clusters [37,38,90] support this qualitative picture. Besides providing further detailed structural information, one major point of discussion in the theoretical contributions is the question, whether multiple adsorption of oxygen onto the small noble metal clusters might occur.

The consequences for the O_2 adsorbate structure, deduced from the frontier orbital picture of Fig. 11, are an O–O bond elongation resulting from the electron transfer (δ^-) into the O_2 π_g^* anti-bonding orbitals. This effect evidently depends on the amount of electron transfer and generates a superoxide, or superoxo (O_2^-)-type adsorbate species. In the case of negatively charged silver and gold clusters, the molecular superoxo structure of the adsorbed oxygen could be confirmed by photoelectron spectroscopic experiments [49,52,53]. It is very particular for the small silver and gold cluster anions that O_2 is bound in a molecular fashion and the strong influence of, e.g., the charge state on the adsorbate structure will be exemplified in the next section. With respect to the consequences for the metal cluster, the electron transfer (δ^-) in the $M_nO_2^-$ complex leads to a depletion of electron density in the M_n^- HOMO which will be identified as an important reason for cooperative adsorption effects.

4.1.2. Charge state dependence—molecular versus dissociative adsorption of dioxygen

The charge state dependent adsorption behavior of O_2 will be discussed for the case of the silver dimer, where detailed information is available for all three-charge states [17,33,34,36,38–40,53]. Neutral Ag_2 has been found to be unreactive toward O_2 in a fast flow reactor at ambient temperature [34], which is not surprising according to the previous discussion considering the paired valence electron structure of Ag_2 (see Fig. 9). Reaction products of Ag_2^- and Ag_2^+ with molecular oxygen obtained in our ion trap are displayed in Fig. 12. The anionic dimer (Fig. 12a) adsorbs one O_2 in a straight forward association reaction similar to the mechanism discussed earlier for the case of Au_2^- (cf. Fig. 7 and Eq. (1)). This is in accordance with the molecular frontier orbital discussion presented in Fig. 11. No further reaction products are detected at any reaction temperature or partial pressure condition in the ion trap [33]. This result is also in agreement with previous flow tube reactor measurements [17] and the molecular superoxo-type bonding of the adsorbate has been confirmed spectroscopically [53].

In contrast, as can be seen from Fig. 12b, the positively charged silver dimer adsorbs at most two oxygen molecules at 50 K reaction temperature [36]. Adsorption of up to three O_2 ligands has been observed recently in a guided ion beam experiment [37]. Calculated geometric structures of the adsorbate complexes presented in the same reference are indicated in Fig. 12b as well. The O_2 binding energies determined from these experiments amount to 0.20, 0.18, and 0.15 eV for the first, second, and third O_2, respectively [37]. In our ion trap measurements, no reaction products $Ag_2O_n^+$ with $n > 4$ are observed for temperatures between 50 and 300 K [36]. However, the distribution of the reaction products reveals a strong temperature dependence (Fig. 13). Fig. 13b and c show two additional product mass spectra obtained at 95 and 130 K reaction temperature. The mass distribution of the products changes drastically at these temperatures. Whereas at 50 K, the exclusive oxidation products $Ag_2O_2^+$ and $Ag_2O_4^+$ point toward molecular adsorption (Fig. 13a), at 95 K, the new product Ag_2O^+ appears and no $Ag_2O_4^+$ is observed anymore. At an even higher temperature of 130 K,

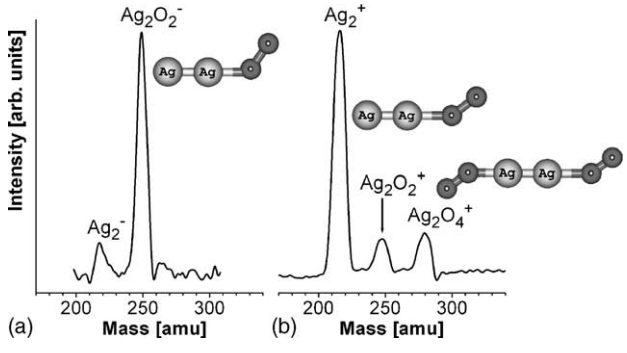

Fig. 12. Product ion mass spectra of silver dimer ion reactions with oxygen in the rf-ion trap. (a) $Ag_2^- + O_2$ at 300 K [33] and (b) $Ag_2^+ + O_2$ at 50 K [36]. The calculated structure for $Ag_2O_2^-$ depicted in (a) is taken from Ref. [33]. The calculated structures of $Ag_2O_2^+$ and $Ag_2O_4^+$ are adapted from Ref. [37].

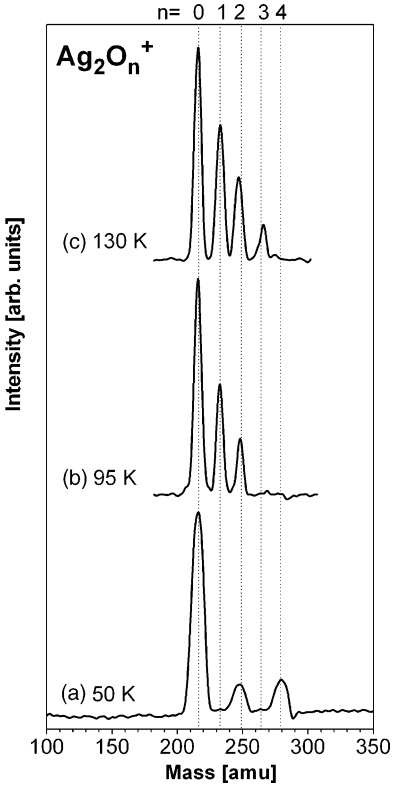

Fig. 13. Product ion mass spectra of the reaction of Ag_2^+ with O_2 at reaction temperatures of (a) 50 K, (b) 95 K, and (c) 130 K [36].

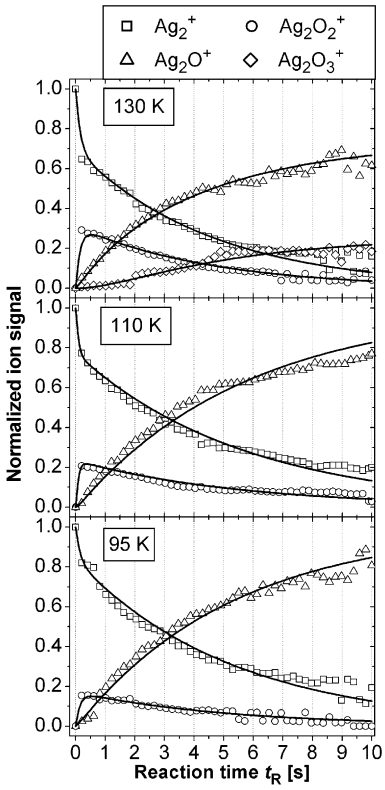

Fig. 14. Product ion concentrations of the reaction $Ag_2^+ + O_2$ as a function of the reaction time t_R for $T = 95$, 110, and 130 K [36]. The open symbols represent the experimental data, normalized on the initial Ag_2^+ concentration and on the total ion concentration in the trap. The solid lines are obtained by fitting the integrated rate equations of the proposed reaction mechanism Eqs. (7a)–(7c) to the experimental data.

$Ag_2O_3^+$ is detected as the largest product. These results indicate a strongly temperature dependent reaction mechanism. In order to extract possible reaction schemes, the reactant and product concentrations are measured as a function of the reaction time. The results for three temperatures (95, 110, and 130 K) are depicted in Fig. 14. The evolution of the Ag_2^+ concentration with reaction time shows a multi-exponential decay at all temperatures. $Ag_2O_2^+$ is identified as an intermediate product with maximum concentration at very short reaction times and increasing amplitude for higher reaction temperatures. The final product at 95 and 110 K is Ag_2O^+, whereas at 130 K the new product $Ag_2O_3^+$ appears with a delay of about 2 s.

These experimental findings suggest the following reaction mechanism:

$$Ag_2^+ + O_2 \rightleftarrows Ag_2O_2^+, \quad k_1, k_2[E_{a,1}, E_{a,2}] \tag{7a}$$

$$Ag_2O_2^+ \rightarrow Ag_2O^+ + O, \quad k_3[E_{a,3}] \tag{7b}$$

$$Ag_2O^+ + O_2 \rightleftarrows Ag_2O_3^+, \quad k_4, k_5[E_{a,4}, E_{a,5}] \tag{7c}$$

k_1–k_5 are the rate constants for the different reaction steps and $E_{a,1}$ to $E_{a,5}$ are the corresponding activation energies. $Ag_2O_2^+$ is unambiguously identified as an intermediate (cf. Fig. 14) and is formed in a first elementary step by molecular adsorption of O_2 onto Ag_2^+. Molecular adsorption of up to two O_2 molecules is also observed at 50 K (Fig. 13a). $Ag_2O_4^+$ is, however, not a stable product at higher temperatures. In a second elementary step, Ag_2O^+ is formed by dissociation of the adsorbed O_2 molecule. The dissociation of O_2 is not observed at 50 K, as the corresponding activation energy is thermally not reached. Increasing the temperature to 130 K results in a further product, $Ag_2O_3^+$. This third elementary step is observed at delayed reaction times and consists of molecular adsorption of O_2 to Ag_2O^+.

The validity of this mechanism is tested by fitting the corresponding integrated rate equations simultaneously to the experimental kinetic data of Ag_2^+ and all observed reaction products as explained in the experimental section. The solid lines in Fig. 14 show that the fitted kinetics of this reaction mechanism describe the experimental data well. In order to further establish this mechanism, other reaction mechanisms were also fitted to the experimental data. We particularly note that purely consecutive reaction steps do not fit the data. This supports the necessity of incorporating equilibrium steps for the reaction of O_2 with Ag_2^+ and Ag_2O^+ and confirms the molecular adsorption of O_2 on these two ions.

Most interestingly, the described temperature dependence of the product ion mass spectra and the obtained temperature dependent kinetics clearly show that, in contrast to the O_2 adsorption on negatively charged silver and gold clusters, the molecular adsorption and the dissociation of O_2 on Ag_2^+ are activated processes. This has been confirmed recently also for the case of larger positively charged silver clusters [38,39,91]. Furthermore, our results allow the construction of the potential energy surface along the reaction coordinate for the established reaction mechanism of the oxidation of silver dimer cations. Fig. 15 shows the proposed reaction path starting with the total binding energy of free Ag_2^+ and O_2, which is defined to be the origin of the energy scale. The corresponding activation barriers are deduced from the

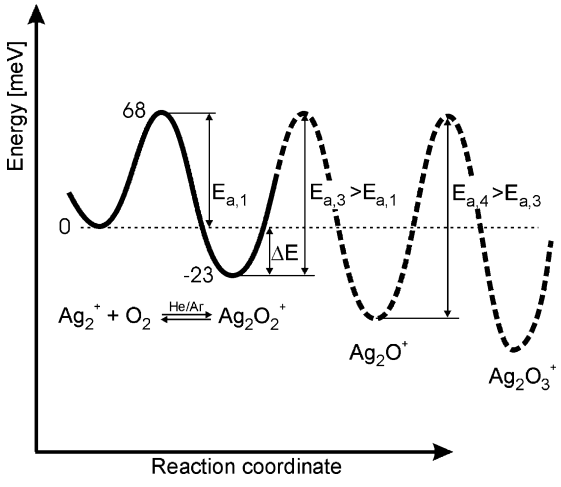

Fig. 15. Schematic potential energy surface along the reaction coordinate for the $Ag_2^+ + O_2$ reaction according to the reaction mechanism of Eqs. (7a)–(7c) and [36].

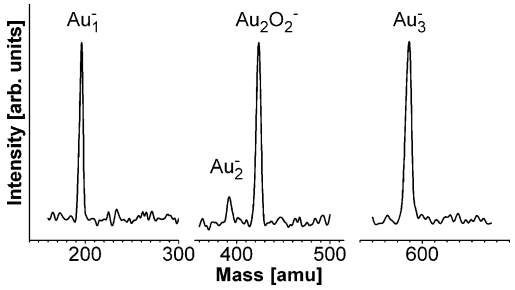

Fig. 16. Product ion distributions analyzed after trapping Au^-, Au_2^-, and Au_3^-, respectively, inside the rf-octopole trap filled with 0.3 Pa O_2 and 1.0 Pa He (200 ms trapping time). Note that no other reaction products are observed even after 10 s trapping period. Reaction temperature, $T = 100$ K [23].

temperature dependence of the rate coefficients according to Arrhenius' equation (Eq. (2)) or are estimated as relative values from the temperature dependent mass spectra [36]. In this particular case of positively charged silver clusters, it is interesting to consider for comparison the O_2 adsorption on single crystal surfaces. For the highly reactive Ag(1 1 0) surface oxygen adsorbs in four different states, depending on the surface temperature: below 40 K, the O_2 is bound in a physisorbed state in the range between 40 and 170 K, it is molecularly chemisorbed, and at higher temperatures, the molecules dissociate on the surface and chemisorb atomically [36,39,92].

4.1.3. Size dependence

The pronounced odd–even size effects in the reactivity of the silver and gold cluster anions with molecular oxygen have been discussed before (cf. Fig. 1). In the following, the reactions of small Au_n^- and Ag_n^- with O_2 in the rf-ion trap under controlled reaction conditions (partial pressures, reaction time, reaction temperature) will be presented. Product ion mass spectra for the reactions of Au^-, Au_2^-, and Au_3^- obtained at 100 K with solely oxygen present as reactive gas in the ion trap are displayed in Fig. 16, [23]. In agreement with the literature, only Au_2^- is found to react [16–18] (Fig. 1). Au^- and Au_3^- do not form any product ions with oxygen. This could be confirmed over the whole temperature range accessible in our experiment. The single product ion of oxygen and Au_2^- is the dioxide $Au_2O_2^-$. The reaction kinetics have been presented and analyzed in the experimental section (see Fig. 7) and a simple association reaction mechanism was deduced [67].

Product ion mass spectra measured after reaction of mass-selected silver cluster anions with oxygen are depicted in Fig. 17a. As in the case of the gold cluster anions, an alternating size dependence is observed. However, the reaction behavior of Ag_n^- is in marked contrast to that of Au_n^- clusters. Whereas Ag_n^- with even n adsorb only one O_2 similar to even n Au_n^-, silver clusters with odd number n of silver atoms adsorb at maximum two oxygen molecules. Ag_4^- even first forms $Ag_4O_2^-$, but then reacts with additional two O_2 molecules at long reaction time and low temperature (cf.

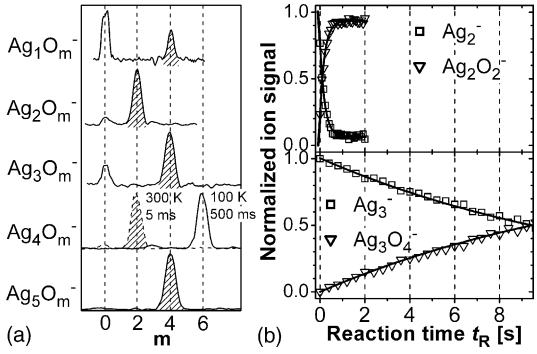

Fig. 17. (a) Product ion mass spectra after reaction of Ag_n^- with O_2. Ion intensities are plotted as function of the number of adsorbed oxygen atoms m. (b) Examples of measured oxidation kinetics for Ag_2^- and Ag_3^- at 300 K. Open symbols: experimental data and solid lines: kinetic fit. Ag_2^-: $p(O_2) = 0.12$ Pa and $p(He) = 1.06$ Pa; Ag_3^-: $p(O_2) = 0.23$ Pa and $p(He) = 1.03$ Pa [33].

Fig. 17a). No products with an odd number of oxygen atoms are detected. The corresponding kinetic data (see Fig. 17b) are best fitted by a sequential adsorption reaction mechanism:

$$Ag_n^- + 2O_2 \xrightarrow{k_1} Ag_nO_2^- + O_2 \xrightarrow{k_2} Ag_nO_4^- \quad (8)$$

The fit of the integrated rate equations is represented by the solid lines in Fig. 17b. The rate constants k_1 and k_2 at 300 K are plotted in Fig. 18a as a function of cluster size. Note that the rates change over at least two orders of magnitude when the size of the clusters is increased by a single atom. Rate constants k_1 for the silver cluster reactions with O_2 have been reported before [17] and these results are in reasonable agreement with our data. However, in the previous report products with more than one O_2 have not been observed for Ag_n^- ($n = 1$–5).

The interesting odd–even trend shown for Ag_n^- ($n = 1$–5) in Fig. 17a also extends to larger cluster sizes [40]. Furthermore, a general increase in silver cluster anion reactivity toward O_2 with increasing size is observed. For the larger sizes ($n \geq 6$), the reactions proceed too fast to be resolved in our experiment. Trace amounts of O_2, which are below the sensitivity of our Baratron pressure gauge (<0.008 Pa), are sufficient to completely oxidize the even numbered clusters with $n \geq 6$ within a few hundred milliseconds.

The sequential adsorption of two oxygen molecules on the odd size clusters takes place without appearance of intermediate products $Ag_nO_2^-$ in the product ion mass spectra recorded at various reaction times (cf. Fig. 17a). This points toward the adsorption of the first O_2 being the rate determining step, whereas the secondary O_2 addition must proceed within the Langevin collision rate limit [69] or at least on a much faster time scale than the resolution of our experiment. Lower limits for k_2 are given in these cases in Fig. 18a. On the other hand, the adsorption of a second O_2 onto Ag_2^- is not observed in the experiment, therefore, an upper limit for the corresponding k_2 value is estimated.

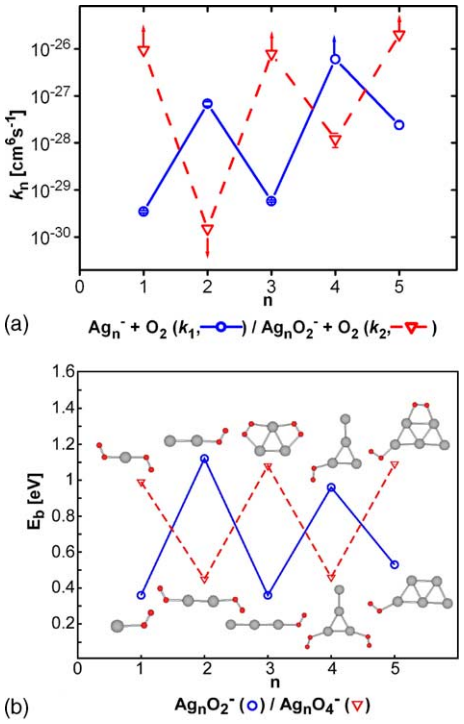

Fig. 18. (a) Experimental termolecular rate constants obtained for the adsorption of the first and second O_2 molecule onto Ag_n^- at $T = 300$ K. (b) Theoretical binding energies E_b and lowest energy structures (grey spheres: silver atoms; dark spheres: oxygen atoms). Note that the lowest energy structures of AgO_2^- and $Ag_3O_4^-$ contain dissociated oxygen (not shown), which however, requires considerable activation energy not available under our experimental conditions [33].

In conjunction with these experimental reaction kinetics results a systematic theoretical study of $Ag_nO_{2m}^-$ clusters in the framework of density functional theory was performed by the group of Bonačić–Koutecký [33,93]. The applied methodology allows to accurately determine structural properties and binding energies, especially when the bonding with oxygen is involved [94]. The resulting theoretical cluster complex structures and binding energies are displayed in Fig. 18b. As can be seen from Fig. 18, the experimentally obtained reaction rate constants (Fig. 18a) compare particularly well with the trend in the calculated O_2 binding energies E_b (Fig. 2b), because, according to statistical rate theory [64,67], E_b largely determines the rate of unimolecular decomposition of the initially formed energized complex (k_d in Eq. (4a)) in the framework of the Lindemann model presented in Section 2.3. The results of the oxygen reaction experiment on silver cluster anions are also in agreement with the frontier orbital picture presented in Section 4.1.1 and this will be used in Section 4.3.2.3 in order to trace the multiple adsorption of O_2 onto Ag_n^- to cooperative adsorption effects on the electronic cluster complex structure.

Finally, all reactions studied display increasing rate constants with decreasing temperature. This negative temperature dependence is indicative for barrierless adsorption pathways as discussed in the experimental section for the case of

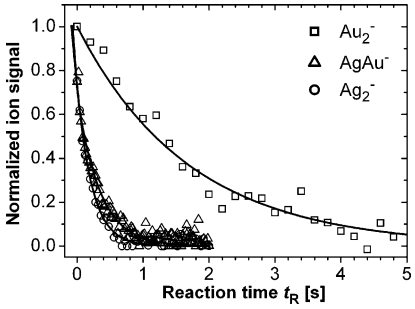

Fig. 19. Kinetics of the reactions of Ag_2^-, $AgAu^-$, and Au_2^- with molecular oxygen. The reaction temperature is 300 K. The oxygen partial pressure in all three measurements amounts to 0.12 Pa. Plotted are the metal cluster ion signal decays in the ion trap as a function of the reaction time t_R. The solid lines represent the fit of the integrated rate equations to the experimental data [70].

Au_2^- in reaction with O_2 [64,67]. It is, however, in marked contrast to the previous investigation of the oxidation mechanism of positively charged silver dimer Ag_2^+, where distinct reaction barriers and temperature dependent reaction pathways could be observed [36].

4.1.4. Composition dependence

Fig. 19 shows the reaction kinetics of the dimer anions Ag_2^-, $AgAu^-$, and Au_2^- with O_2. For comparison, the decays of the metal cluster ion concentrations are plotted only. Interestingly, there is almost no difference between the reaction rates of the dimers Ag_2^- and $AgAu^-$ with oxygen. Au_2^-, in contrast, reacts considerably slower [70]. Hence, the change in chemical reactivity toward O_2 with composition is not linear. This is also in accord with the fact that the VDE of $AgAu^-$ is closer to the VDE value of Ag_2^- than to that of Au_2^- (cf. Fig. 8, [73]). The unanticipated and discontinuous change of reactivity with the composition of the small clusters is even more pronounced for the trimer anions, because both Ag_2Au^- and $AgAu_2^-$, do not react with O_2 at all under our experimental conditions, similar to Au_3^- [95]. A quantitative comparison of the obtained rate constants will be presented together with the CO reaction rate constants in Section 4.2.4.

4.2. CO adsorption

4.2.1. Molecular orbital model of CO adsorption

The bonding of CO (carbonyl) ligands in complexes with transition metals is typically classified into several components. Apart from the electrostatic interaction, the major contributions are explained classically within the σ donation and π back-donation model: The $s\sigma^*$ (also commonly labeled 5σ) electron of the CO molecule donates to the metal valence σ symmetry orbital and the metal dπ electron back-donates to the $2p\pi^*$ orbital of CO (see Fig. 20). Very minor contributions from a π donor interaction between a pπ CO electron and open metal π orbitals are in general neglected [96]. CO bonding is, therefore, particular favorable for elements with

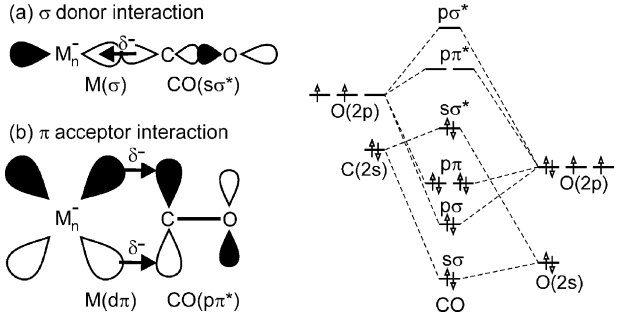

Fig. 20. Left: schematic MO picture of the interaction of carbon monoxide with silver and gold cluster anions M_n^-. Major bonding contributions are (a) σ donation of charge (δ^-) from the filled CO sσ* anti-bonding orbital into the LUMO of the metal cluster anions and (b) π back-donation from metal cluster d orbitals into the empty pπ* anti-bonding orbitals of CO. Right: schematic, rudimentary MO energy level diagram for CO which can be refined by inclusion of s, p-mixing. Even in its simplest form, the nature of the HOMO (σ*, anti-bonding) and the LUMO (π*, anti-bonding) is depicted correctly [96].

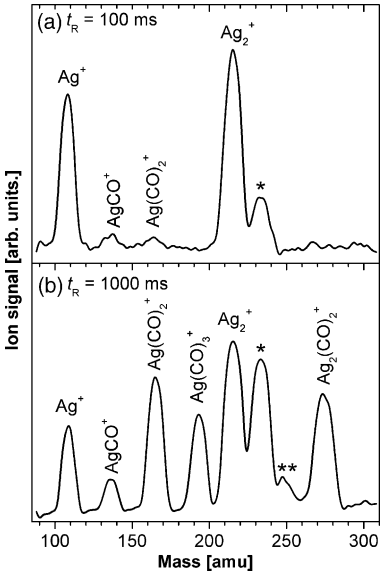

Fig. 21. Product ion mass spectra of the reaction of Ag_2^+ with CO in the ion trap obtained at two different reaction times (T = 300 K and p(CO) = 0.9 Pa): (a) t_R = 100 ms and (b) t_R = 1000 ms. The peak labeled with an asterix corresponds to $Ag_2(H_2O)^+$, the one with double asterix to other unassigned impurities. Note that in contrast to the strong reaction and fragmentation observed for Ag_2^+, the negatively charged silver clusters do not react with CO at all [103].

partially occupied d shells, i.e., with an empty dσ acceptor orbital and a filled dπ donor orbital. For the case of group Ia metals, however, carbonyls are only weakly bound, because the d shell is fully occupied. Carbonyl σ donation is possible only into an sσ or a pσ metal orbital and π back-donation into the CO pπ* orbital is not very favorable because of the generally low energy of the d orbitals, in particular for silver [17,97].

The model of CO bonding to silver and gold clusters emerging from these ideas mainly considers two factors: (i) the cluster highest occupied molecular orbitals and lowest unoccupied molecular orbitals (LUMOs) are constructed from metal s orbitals. Calculated LUMO energies for silver and gold clusters are in energy considerably above the HOMO [31,72,81,82,98] (cf. also Fig. 10). Therefore, electron donation from the 5s orbital of CO to the cluster LUMO will provide only a slightly attractive interaction in the case of anions [17], which is, however, expected to increase considerably when going to the neutral or even cationic clusters according to recent calculations [99]. The charge state thus determines the contribution of σ donation to the noble metal cluster CO bonding. (ii) The back-bonding from a metal dπ orbital, or from a cluster molecular orbital of the appropriate symmetry to the CO 2pπ* anti-bonding orbital leads to an attractive interaction. The importance of π back-donation to the CO bonding is supported by spectroscopic studies on matrix-isolated small silver and gold cluster carbonyls [97,100]. The contribution of π back-donation bonding thus depends on the relative energetic location of the metal d orbitals, i.e., on the metal cluster composition.

The charge state, size, and composition dependent reactivity of silver and gold clusters toward CO is influenced by the energy differences between the metal valence d-, s-, and p-derived orbitals which is in contrast to the O_2 bonding (Fig. 11), where the s orbital derived HOMO was identified to be of principal importance. This might explain the different cluster size dependent reactivity of the silver and gold clusters toward the two reactants reported in Fig. 1.

4.2.2. Charge state dependence

In matrix isolation experiments, carbonyls of atomic silver and gold in positive and neutral charge state have been identified [97,100,101]. However, in case of the neutral complexes, only for AuCO σ donation and π back-donation are operative, and thus AgCO is found to be unstable [102]. In agreement with these results, gas-phase reactivity measurements showed the formation of Au_2CO, but not of Ag_2CO [34]. CO reactivity results for larger positively charged or neutral silver clusters are not available. According to the bonding model presented above, the bonding between the clusters and CO is related to the balance between the CO to metal electron donation and the metal to CO back-donation. The CO to metal σ donation is expected to be stronger for the cation than for the neutral atom. Similarly, the forward donation for the neutral will be stronger than for the anion, as indicated in recent calculations [99]. In our ion trap measurements, CO is found to react strongly with Ag_2^+ leading to fragmentation as can be seen from the product ion mass spectra presented in Fig. 21 [103]. Already after 100 ms, the fragment ion Ag^+ is observed, which itself also further reacts with up to three CO molecules at longer reaction times (Fig. 21b). This is in agreement with matrix isolation reaction experiments [101]; in guided ion beam experiments, adsorption of up to four CO on Ag^+ was detected [104]. The only product ion observed in the ion trap for Ag_2^+ is $Ag_2(CO)_2^+$ (Fig. 21b), which means that adsorption of the first CO is the rate determining step in the sequential formation of $Ag_2(CO)_2^+$. AgCO is not stable, as mentioned above. Finally, silver cluster anions do not

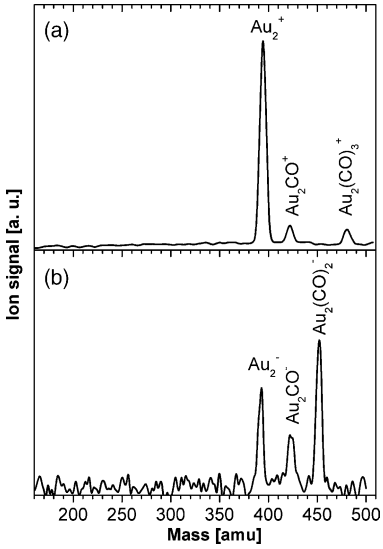

Fig. 22. Product ion mass spectra of gold dimer ion reactions with CO in the ion trap. (a) Au_2^+ + CO (T = 70 K, trace amounts of CO, p(He) = 1.13 Pa, and t_R = 1 s [14]). (b) Au_2^- + CO (T = 100 K, p(CO) = 0.24 Pa, p(He) = 0.96 Pa, and t_R = 1 s [66]). Note that no fragmentation is observed in the case of the gold dimer.

react with CO under any reaction condition in our ion trap and are also found unreactive in flow tube reactor measurements [17]. This can be understood by considering the above statement that CO to metal σ donation is very weak, if not repulsive, for the negatively charged silver and gold clusters in combination with the fact that the low energy of the silver d orbitals compared to gold means that π back-bonding is especially unfavorable for silver, preventing bonding of the silver cluster anions with CO [17,40].

Fig. 22a displays the product ion mass spectrum of Au_2^+ in reaction with trace amounts of CO at 70 K in the ion trap. Under these conditions, Au_2CO^+ as well as $Au_2(CO)_3^+$ are observed. Supposed that a sequential adsorption mechanism prevails, the rate-determining step in this case is the adsorption of the second CO molecule. The formation of carbonyls of larger gold cluster cations has been observed in an ICR mass spectrometer [24]. The neutral $Au_2(CO)_2$ has been detected again spectroscopically in matrix isolation experiments [100]. For gold, strong relativistic effects lead to a decrease in s–d orbital distance making the d derived molecular cluster orbitals available for π back-donation. Therefore, although carbonyls of the atomic gold anion are not observed, due to repulsion of the doubly occupied metal s orbital and the donating CO sσ* orbital, the formation of carbonyls for all larger Au_n^- have been reported with different experimental approaches [17,23,25,26,66,105]. Fig. 22b shows the product ion mass spectrum of Au_2^- in reaction with CO in the ion trap. The detailed reaction kinetics and the cluster size dependence of the CO adsorption kinetics of the small Au_n^- clusters will be discussed in the next section.

4.2.3. Size dependence—influence of internal degrees of freedom

A very striking size effect on the kinetics of previously unknown small gold cluster carbonyls will be presented in the following. Particular emphasis in the discussion will be put on the correlation between electronic structure and carbonyl complex stability as well as on the influence of the number of internal degrees of freedom on the reaction kinetics [66]. In our experiment, no reaction products of Au_n^- (n = 1–3) with CO are detected at temperatures above 250 K. This is in agreement with earlier reports, which investigated the size dependent reactivity of Au_n^- with CO and did observe gold anion carbonyls only for clusters with $n \geq 4$ [25,26]. At lower temperatures, still no reaction products for the monomer are found, due to metal s and CO sσ* orbital repulsion, as explained above. Cooling of the rf-ion trap to temperatures below 250 K leads in the case of Au_2^- and Au_3^- first to the formation of the monocarbonyls and at the lowest temperatures to a maximum adsorption of two CO molecules as can be seen from the lower traces in Fig. 23.

In order to deduce the reaction mechanism of the observed reactions, the reactant and product ion concentrations as a function of reaction time are recorded. The resulting kinetic traces for Au_2^- as well as for Au_3^- at 100 K reaction temperature are depicted in Fig. 24. The open symbols represent the experimental data normalized to the total ion concentration in the trap during reaction. The kinetic traces of Au_2^- and Au_3^- have a strikingly different appearance. This is even more pronounced considering that the reactive gas concentration in the ion trap in Fig. 24b (Au_3^-) is less that one tenth of the CO concentration in Fig. 24a (Au_2^-). In both cases, the Au_n^- signal decreases exponentially, but the carbonyl product concentrations show very different evolution as a function of reaction time. In the case of Au_3^-, the monocarbonyl can clearly be identified as an intermediate with decreasing concentration at longer reaction times, whereas for Au_2^- the mono- and di-carbonyl concentrations rise simultaneously to reach equilibrium.

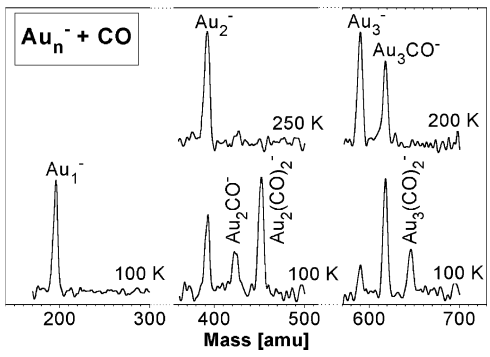

Fig. 23. Product ion distributions analyzed after trapping Au^-, Au_2^-, and Au_3^-, respectively, inside the octopole trap filled with 1 Pa of helium and a small partial pressure of carbon monoxide. Reaction temperatures are as indicated. Note that no other reaction products are observed even after 10 s trapping period [66].

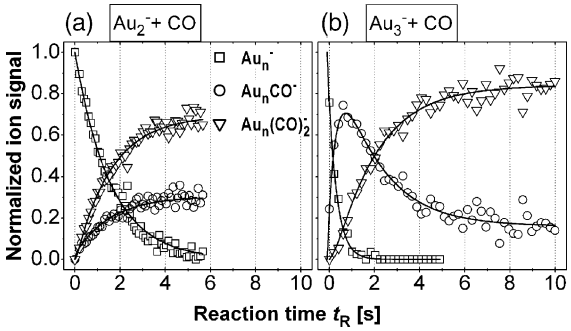

Fig. 24. Kinetic traces of the reaction of (a) Au_2^- and (b) Au_3^- with CO at a reaction temperature of 100 K. Plotted are the product ion concentrations as a function of the reaction time t_R. The open symbols represent the normalized experimental data. The solid lines are obtained by fitting the integrated rate equations of the reaction mechanism Eqs. (9a) and (9b) to the experimental data. The partial pressures are (a) p(He) = 0.96 Pa and p(CO) = 0.24 Pa; (b) p(He) = 1.08 Pa and p(CO) = 0.02 Pa.

Most interestingly, the kinetics of both, Au_2^- as well as Au_3^-, are best fit by the same mechanism. This reaction mechanism is represented by the following equations:

$$Au_n^- + CO \xrightarrow{k_1} Au_nCO^- \quad (9a)$$

$$Au_nCO^- + CO \underset{k_{-2}}{\overset{k_2}{\rightleftarrows}} Au_n(CO)_2^- \quad (9b)$$

k_1, k_2, and k_{-2} are the rate constants for the different reaction steps. The adsorption of CO occurs sequentially with Au_nCO^- as an intermediate product. Purely consecutive reaction steps do not fit the experimental data and it is, therefore, essential to introduce a final equilibrium (Eq. (9b)). The fits to the data are represented by the solid lines in Fig. 24 and are an excellent match to the experimental results. The corresponding rate constants are listed in Table 2. Note that the measured rate coefficient for the reaction of the first CO with a gold cluster anion $k_1^{(3)}$ is more than 44 times larger for the trimer than for the dimer cluster anion.

Castleman and co-workers pointed out the important relation between the product formation rate and the possibility of intracluster energy redistribution, which is reflected by the number of internal vibrational degrees of freedom, for gas-phase metal cluster reactions [106]. In the case of positively charged copper clusters, this group observed a minimum number of seven atoms necessary for the cluster to form its own heat bath, and thus to be able to accommodate the excess energy released during CO adsorption. Above seven atoms per cluster, the reaction rate coefficients as a function of the number of atoms per cluster did not change significantly. However, this function showed the most dramatic increase going from the dimer to the trimer cluster. This might be rationalized considering that the dimer has only one internal coordinate, whereas for the trimer, the cluster potential energy surface becomes at least three-dimensional which is a drastic change in terms of the possibility of internal energy redistribution. Hence, the observed pronounced increase of the reaction rate going from the gold dimer to the trimer ion is expected to be intimately related to the rising number of internal degrees of freedom.

In order to further quantify this conclusion, the Lindemann energy transfer model for association reactions presented in Section 2.3 has to be considered. Under the experimental conditions of the ion trap experiment, the termolecular rate constant is represented by Eq. (6). The association rate constant k_a as well as the final stabilization rate constant k_s is, however, basically cluster size independent according to Langevin theory [68,106]. The cluster size dependence of $k^{(3)}$, is thus contained in the unimolecular decomposition rate constant k_d of the metastable intermediate complex. In order to estimate k_d, Rice–Ramsperger–Kassel-theory is employed [66]. The RRK decomposition rate constant is [64]

$$k_d = \nu\left(\frac{E - E_0}{E}\right)^{S-1} \quad (10)$$

for the given case that the total internal energy E, contained in S independent oscillators, is larger than the CO binding energy to the gold cluster E_0. ν is the frequency factor [107], which can be considered identical for the dimer and the trimer ion.

If also the assumption is made that the CO binding energies to Au_2^- and Au_3^- are similar, which is very reasonable according to recent theoretical work [46,89,99,108], the ratio of the termolecular rate constants can be calculated [66]:

$$\frac{k^{(3)}(Au_3^-)}{k^{(3)}(Au_2^-)} = \frac{k_d(Au_2^-)}{k_d(Au_3^-)} = \frac{(E_0 + 6k_BT)^8}{2^8(3k_BT)^3(E_0 + 3k_BT)^5} \quad (11)$$

Taking the experimental reaction temperature of T = 100 K and the measured rate constant ratio of 44, the CO binding energy E_0 on the small gold clusters can be obtained: $E_0 \approx 0.5$ eV. Note that this estimated value represents a mean value between the assumed similar CO binding energies to Au_2^- and Au_3^-. This binding energy compares well to known experimental as well as theoretical values [46,89,99,105]. Also the adsorption energy of CO on an extended Au(3 3 2) surface has an energy in the same range (0.57 eV) [109]. This good agreement supports the outstanding importance of the increasing number of degrees of freedom, on which the RRK model is exclusively based, on the

Table 2
Rate constants according to Eqs. (9a) and (9b) for the adsorption reactions of carbon monoxide onto the gold dimer and trimer anion clusters

Cluster	$k_1^{(3)}$ (10^{-29} cm^6 s^{-1})	$k_2^{(1)}$ (s^{-1})	$k_{-2}^{(1)}$ (s^{-1})	$K = k_2^{(1)}/k_{-2}^{(1)}$
Au_2^-	0.52 ± 0.03	13.2 ± 1.0	5.8 ± 0.8	2.3
Au_3^-	23 ± 6	0.45 ± 0.12	0.087 ± 0.023	5.2

Also listed are the equilibrium constants K for the final reaction step Eq. (9b).

rate coefficients. Hence, the factor of 44 higher rate coefficients for the trimer reaction with CO can be largely ascribed to the considerably more efficient internal energy redistribution after initial CO adsorption in Au_3^- than in Au_2^-.

The reaction kinetics of Au_2^- and Au_3^- in Fig. 24 appear clearly dissimilar, although they can be described by the same underlying reaction mechanism (Eqs. (9a) and (9b)). Further inspection of Table 2 shows that the dissimilarity is due to the different ratio (k_2/k_{-2}) of the adsorption and desorption rate coefficient of the second CO molecule for Au_2^- and Au_3^-. $K = k_2/k_{-2}$ is the equilibrium constant of the reaction in Eq. (9b). K is larger than one for both cluster sizes, but the equilibrium is located by a factor of 2.3 more on the side of the final product $Au_3(CO)_2^-$ than on $Au_2(CO)_2^-$ (cf. Table 2). This points toward a significantly higher stability of $Au_3(CO)_2^-$ compared to all the other investigated carbonyl compounds. To explain the enhanced stability of certain free gold carbonyls, a simple electron-counting scheme was suggested by other groups [24,25]. In this picture, $Au_3(CO)_2^-$ would correspond to a stable eight electron complex. However, recent theoretical investigations emphasize the importance of sd hybridization due to relativistic effects in gold clusters [81]. Hence, the role of the d-electrons on the bonding in gold carbonyl complexes must not be neglected (cf. also Sections 3 and 4.2.1) and an s-electron based delocalized-shell-type explanation of the complex stability is not justified [81]. Another possible explanation for the comparably large adsorption rate of CO onto Au_3CO^- might be found in cooperative bonding effects leading to a structural isomerization of the trimer from the linear to a triangular structure induced by the adsorption of the first CO molecule. Recent quantum chemical calculations [89] suggest that the binding energy of the second CO to a triangular Au_3^- core is about 50% larger than to a linear gold trimer in Au_3CO^- (1.44 eV compared to 0.85 eV). Binding energies of the first and second CO to the linear Au_3^- are, however, comparable. It might, therefore, be speculated that the adsorption of the first CO onto the linear Au_3^- leads to a charge transfer from the gold cluster to the CO molecule via the π back-donation mechanism. As a consequence of the reduced electron charge on the metal trimer, an isomerization to a triangular structure is induced [110], which in turn favors the adsorption of the second CO molecule. The reaction of this complex with a third CO molecule has been predicted theoretically [89], but is not observed in our experiment [66]. Similar adsorbate induced electronic changes will be important for the coadsorption effects discussed below.

4.2.4. Composition dependence—influence of relativistic effects

The experimentally deduced rate constants $k^{(3)}$ for all cluster ions $Ag_nAu_m^-$ with $(n+m) = 1$–3 in reaction with CO as well as O_2 are summarized in Fig. 25. All observed adsorption reactions show the discussed negative temperature dependence. As explained previously, silver and gold atomic ions do not react with CO and only Ag^- reacts with O_2 (Fig. 25a).

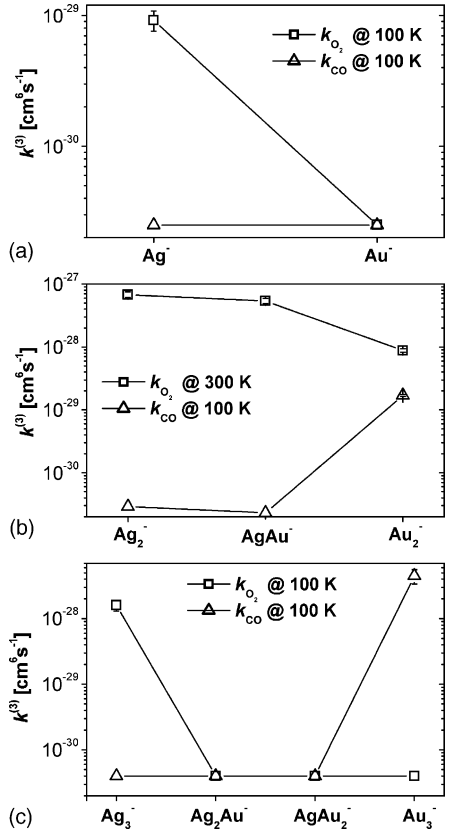

Fig. 25. Experimental reaction rate constants $k^{(3)}$ for all cluster ions $Ag_nAu_m^-$ with $(n+m) = 1$–3 in reaction with CO as well as O_2. All observed adsorption reactions show a negative temperature dependence. In the cases where no reaction products were observed in the mass spectra, the estimated detection limit of the ion trap experiment is plotted ($\approx 3 \times 10^{-31}$ cm^6 s^{-1}) [70].

For the dimer anions, the trend in reactivity toward CO is contrary to the reactive behavior toward O_2 (Fig. 25b). Ag_2^- and $AgAu^-$ do not react, i.e., the reaction rate constants are below the detection limit of the ion trap experiment, which is around $k^{(3)} \approx 3 \times 10^{-31}$ cm^6 s^{-1}. Only Au_2^- shows measurable reactivity toward CO (Fig. 25b).

Again, the bonding can be understood based on the energy differences between valence orbitals of the metal atoms and clusters. The reactivity toward O_2 is determined by the relative energetic location of the metal cluster HOMO (Section 4.1.1), whereas the bonding capability of the silver and gold cluster anions toward CO is mainly related to the energetic location of the metal cluster d-type orbitals (cf. Section 4.2.1). In changing the cluster composition from pure silver to gold atom by atom, the influence of relativistic effects on the chemistry of the clusters introduced by the increasing gold content can be investigated. Qualitatively, the relativistic effects include the contraction and stabilization of the s and p shells, as well as an expansion and destabilization of the d atomic orbitals [34]. The latter is an indirect effect due to more efficient screening by the contracted s and p shells. Exactly this destabilization of the gold d orbitals would be expected to increase their availability for π back-donation in Au_n^-

association complexes resulting in the stronger bonding observed. In contrast, in silver cluster anions, the d orbitals lie much deeper below the s orbitals than in gold, consequently the carbonyl complexes relying on a π back-donation are significantly less stable [34] and not observed in our experiment. The fact that $AgAu^-$ does not react with CO, similar to Ag_2^-, implies that the relativistic d orbital destabilization in the mixed dimer is not sufficient and that the d-type orbitals of $AgAu^-$ are still not energetically available for CO π back-bonding which is qualitatively in contradiction to the calculated results depicted in Fig. 10, [82].

In our ion trap experiment, no reactions of Ag_n^- with CO were observed between 100 and 300 K for any cluster size up to 11 atoms per cluster. Also in the earlier investigation, no reaction products of silver cluster anions with carbon monoxide were reported [17]. These differences in CO interactions with silver and gold are also apparent in adsorption of CO on the bulk metal surfaces which supports the fact that the valence dπ orbital in silver is extremely stable compared to the same orbital in gold atoms and that the π back-donation bonding in silver is not efficient. Heats of adsorption for CO at low coverage are 27–42 kJ mol^{-1} for silver [111] and 55–58 kJ mol^{-1} for gold [109,112].

In the case of the trimer anions, it is even more apparent that the influence of relativistic effects is not necessarily proportional to the gold content. The binary trimer anions both neither react with O_2 nor with CO (Fig. 25c). This means that by exchange of a single silver atom in Ag_3^- to Au, the cluster becomes essentially unreactive toward oxygen. The same is true for the reactivity toward carbon monoxide when one gold atom in Au_3^- is exchanged by a silver atom. Apparently, in the latter case, already one silver atom leads to a high stabilization of the metal cluster d orbitals making them energetically unavailable for CO π back-bonding. On the other hand, the high VDE values (cf. Fig. 8) of all trimer anions compared to Ag_3^- (which itself already binds O_2 very weakly only [33]) are in line with their unreactivity toward the electron acceptor O_2.

Adsorption measurements with O_2 and CO, therefore, seem to be suitable to draw qualitative conclusions about the relative locations of the cluster electronic s and d levels under the influence of relativistic effects.

4.3. Cooperative coadsorption effects

Coadsorption phenomena in heterogeneous catalysis and surface chemistry quite commonly consider competitive effects between two reactants on a metal surface [41,42]. Also cooperative mutual interaction in the adsorption behavior of two molecules have been reported [41]. Recently, this latter phenomenon was found to be very pronounced on the small metal cluster ions too [15,23,27,113]. This is mainly due to the fact that the metal cluster reactivity is strongly charge state dependent as discussed above and that an adsorbed molecule can effectively influence the metal cluster electronic structure by, e.g., charge transfer effects (cf. Figs. 11 and 20). This changed electronic complex structure, in term, might foster (or also inhibit) adsorption and reaction of further reactant molecules that would otherwise not be possible. Three examples of cooperative adsorption effects on small silver and gold cluster ions identified in our ion trap experiments will be presented in the following. The cases of either CO or O_2 preadsorption will be distinguished.

4.3.1. CO preadsorption

Au_3^- does not react with O_2 in the ion trap at any reaction temperature (Fig. 16). It adsorbs a maximum of two CO molecules at reaction temperatures below 250 K (Fig. 23). If the gold trimer is exposed simultaneously to CO and O_2 inside the octopole ion trap, still no reaction products are observed at reaction temperatures above 250 K as can be seen from Fig. 26a. Fig. 26b shows that at 200 K one CO molecule adsorbs onto Au_3^-. Further cooling, however, does not lead to adsorption of a second CO molecule as has been seen when only carbon monoxide is in the trap, but instead results in the additional adsorption of up to two O_2 molecules under formation of the coadsorption products $Au_3(CO)O_2^-$ and $Au_3(CO)(O_2)_2^-$ (Fig. 26c) [23]. Hence, the adsorption of CO onto Au_3^- seems to change the cluster complex electronic structure in a way that it is now able to react with oxygen. In other words, CO preadsorption conditions the gold cluster to enable O_2 coadsorption. This temperature dependent product formation demonstrates that first one CO has to be adsorbed onto the gold cluster before subsequent O_2 adsorption becomes possible.

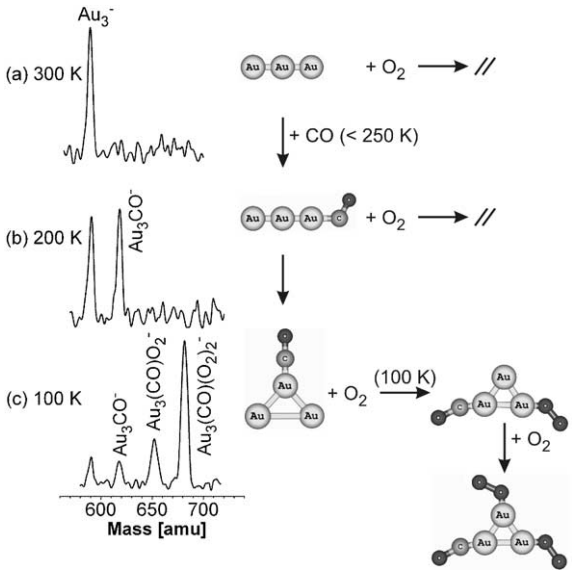

Fig. 26. Temperature dependent mass spectra of the reaction of Au_3^- with O_2 and CO. The product ion distributions are analyzed after trapping Au_3^- for 500 ms inside the octopole ion trap filled with 0.02 Pa O_2, 0.05 Pa CO, and 1.23 Pa He. Reaction temperatures: (a) 300 K, (b) 200 K, and (c) 100 K [14,23]. The proposed cooperative adsorption mechanism is indicated schematically (see text for details). Large grey spheres indicate gold atoms, small dark gray spheres carbon atoms, and dark spheres oxygen atoms.

The following idea for a possible molecular mechanism of this unexpected cooperative action of two adsorbate molecules on the small Au_3^- cluster is based on recent ab initio simulations of CO adsorption and CO/O_2 coadsorption energetics and structures [89] as well as on previous experiments on the femtosecond dynamics of noble metal clusters initiated by a change of the charge state [32,110,114]. At temperatures below 250 K, Au_3^- adsorbs CO under our experimental conditions. The interaction of the first CO molecule proceeds mainly through π back-bonding leading to a charge transfer from the metal cluster to the CO molecule as depicted in Fig. 20. From femtosecond laser spectroscopic investigations, it is known that the initially linear noble metal trimer anions undergo bending motion to reach a triangular geometry, if the additional charge is reduced [110]. Therefore, it is likely to assume that the CO adsorption might lead to a change in the cluster complex geometry as depicted schematically in Fig. 26. According to the theoretical simulations, the linear Au_3CO^- has a high VDE of 3.37 eV and does not form stable complexes with O_2 [89]. The triangular Au_3CO^- complex, however, exhibits a considerably lower VDE of only 2.83 eV [89] and is, therefore, predicted to react with oxygen under formation of the coadsorption complex $Au_3(CO)O_2^-$, which has indeed been observed experimentally. Also the formation of $Au_3(CO)(O_2)_2^-$ is confirmed by this calculations [89] (cf. Fig. 26). Hence, the observed cooperative adsorption on Au_3^- might be attributed to an adsorbate induced geometry change of the metal cluster which in turn results in a reduced HOMO energy (lower VDE) enabling the subsequent O_2 adsorption.

4.3.2. O_2 preadsorption

4.3.2.1. $Au_2(CO)O_2^-$. Au_2^- reacts more than one order of magnitude faster with O_2 than with CO. Accordingly, when the octopole ion trap is filled with similar partial pressures of both reactive gases, O_2 adsorption will most likely precede CO adsorption [67]. Product ion distributions at two different temperatures for the case when O_2 and CO are present in the trap are depicted in Fig. 27. As can be seen from these mass spectra, the dimer Au_2^- forms the dioxide at 300 K, but a new additional peak at the mass of $Au_2(CO)O_2^-$ appears at a temperature of 100 K (hatched peak in Fig. 27b). This is the final, major reaction product, which shows that Au_2^- clearly favors the simultaneous coadsorption of both, oxygen and carbon monoxide, over adsorption of just one sort of reactive molecule [23]. This kind of cooperative effect was also found for larger gold cluster anions in a flow-reactor study [27]. Furthermore, under the conditions of our experiment (Fig. 27b), small amounts of $Au_2O_2^-$ are present too. But most interestingly, no Au_2CO^- or $Au_2(CO)_2^-$ carbonyls are observed at any temperature or reaction time, although these complexes are stable products at cryogenic temperatures. The absence of carbonyl complexes can be rationalized by the above-mentioned observation that the reaction of Au_2^- with oxygen appears to be considerably faster than with carbon monoxide.

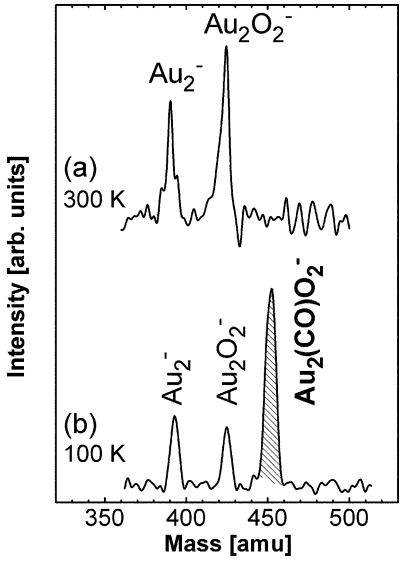

Fig. 27. Temperature dependent mass spectra of the reaction of Au_2^- with O_2 and CO. The product ion distributions are analyzed after trapping Au_2^- for 500 ms inside the octopole ion trap filled with 0.02 Pa O_2, 0.05 Pa CO, and 1.23 Pa He. (a) At a reaction temperature of 300 K, only Au_2^- and $Au_2O_2^-$ are detected. No further ion signals are observed at temperatures above 200 K. Cooling down further reveals an additional ion signal appearing at the mass of $Au_2(CO)O_2^-$ (hatched peak). Mass spectrum (b) shows the ion distribution at 100 K [67].

4.3.2.2. $Ag_n(CO)O_2^-$. Also in the case of selected even size Ag_n^- clusters coadsorption complexes similar to $Au_2(CO)O_2^-$ could be detected. For Ag_4^-, at low oxygen partial pressure and high carbon monoxide partial pressure, a new peak in the product ion mass spectrum could be identified at 100 K. The mass spectrum is depicted in Fig. 28a and the hatched peak corresponds to the species $Ag_4(CO)O_2^-$. In this case, preadsorption of O_2 onto the cluster again clearly promotes subsequent CO coadsorption, because Ag_n^- clusters are not found to react at all with CO only. Fig. 28b shows the mass spectrum recorded after Ag_6^- to Ag_8^- reacted with oxygen and carbon monoxide in the ion trap. Coadsorption is detected for Ag_6^-, yielding the species $Ag_6(CO)O_2^-$ (hatched peak).

4.3.2.3. $Ag_nO_4^-$. In this section, the adsorption of multiple oxygen molecules onto the odd size Ag_n^- clusters described in Section 4.1.3 will be related to cooperative adsorbate effects. Adsorption of two O_2 molecules as observed in our experiment for Ag_n^- (Fig. 17) had been predicted before for the gold cluster anions [88], however, it was never observed experimentally which lead to further discussion in the literature [115]. In combination with a systematic theoretical study performed by the group of Bonačić–Koutecký [33], an understanding of the measured rate constant evolution with cluster size depicted in Fig. 18a emerges and reasons for the distinct behavior of silver cluster anions can be given [33].

The results concerning multiple adsorption of O_2 onto the anionic silver clusters according to Eq. (8) can be assessed by qualitative frontier orbital considerations for the binding of

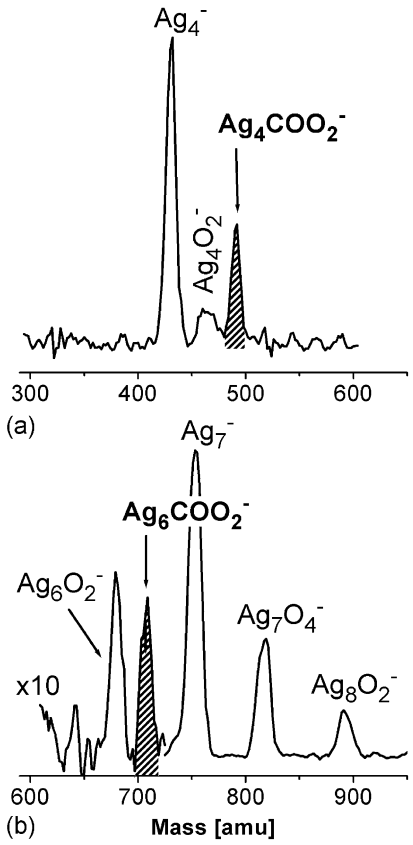

Fig. 28. Coadsorption products observed in the mass spectra after reaction of Ag_4^- and Ag_6^- with O_2 and CO at $T = 100$ K. (a) Ag_4^-: $p(O_2)$ = trace amounts, $p(CO) = 0.03$ Pa, $p(He) = 1.25$ Pa, and $t_R = 2$ s. (b) Ag_{6-8}^-: $p(O_2) = 0.01$ Pa, $p(CO) = 0.03$ Pa, $p(He) = 1.17$ Pa, and $t_R = 0.1$ s.

molecular oxygen as discussed in Section 4.1.1 (Fig. 11). The oxygen molecule, as an one electron acceptor, binds strongly to the anionic silver clusters with odd number of electrons (even n) and low VDE values leading to a small k_d, and hence to a fast reaction rate $k^{(3)}$ in the framework of the Lindemann model (Eqs. (4a), (4b) and (5)). In contrast, it binds only weakly to silver clusters with even number of electrons (odd n) and closed shell electronic structure resulting in low reaction rates $k^{(3)}$ in these cases as can be seen from Fig. 18a. However, recent work on reactivity of hydrated anionic gold clusters with molecular oxygen has shown that this behavior can be inverted by binding of a strong electron acceptor such as the OH group [94]. Due to the electron withdrawing effect, electron transfer from the cluster occurs leaving an unpaired electron on the clusters with even number of electrons and inducing subsequent stronger binding of the molecular oxygen to hydrated clusters.

An analogous mechanism is proposed for the activation of molecular oxygen and the cooperative binding of two oxygen molecules on the anionic silver clusters in which the first adsorbed O_2 serves as an activator [33]. Since anionic silver clusters have generally lower VDE values than gold clusters (cf. Fig. 8), weaker electron acceptors such as O_2 can already induce electron transfer and activate them which is not possible in the case of Au_n^-. The first oxygen molecule is bound to the silver clusters with even number of electrons by 0.36, 0.36, and 0.53 eV for Ag^-, Ag_3^-, and Ag_5^-, respectively [33]. The mechanism of the bonding involves the electron transfer from the metal cluster into the π^* MO of O_2 as depicted in Fig. 11. The binding of the first O_2 molecule changes the electronic structure of the cluster and induces a stronger cooperative binding with the second O_2. This results in the case of Ag_3^- and Ag_5^- in new oxide species with doubly bound, superoxo-like O_2 subunits as can be seen from the calculated structures in Fig. 18b. The cooperative effect is reflected in larger binding energies as shown also in Fig. 18b. Moreover, the binding of the second molecular oxygen shows a reversed pattern being stronger for clusters with odd number of atoms and weaker for the ones with even number of atoms. The latter ones with one unpaired electron bind strongly only one oxygen molecule since the electron transfer leaves them with a closed shell electronic structure. The above mechanism can be extended to the absorption of three oxygen molecules, which should qualitatively exhibit the similar behavior as the adsorption of one O_2. Adsorption of three O_2 molecules has indeed been detected experimentally for Ag_4^- (cf. Fig. 17a).

Hence, experimental rate constant measurements in combination with theoretical simulations show a pronounced size and structure selective activity of anionic silver clusters toward molecular oxygen due to cooperative effects. In particular, for Ag_n^- clusters with odd n a weakly bound first O_2 promotes the adsorption of a second O_2 molecule which is then (for $n = 3$ and 5) differently bound with the O_2 bond elongated to 1.32 Å, and thus potentially activated for further oxidation reactions such as CO combustion which will be investigated in the following section.

5. Catalytic CO oxidation

The possible catalytic activity of Au_2^- in the CO combustion reaction was first predicted by Häkkinen and Landman [46]. Our subsequent experimental investigation indeed revealed the catalytic reaction of the gold dimer and, in conjunction with theory, a detailed reaction cycle could be formulated [67]. Also for particular larger gold cluster anions evidence for catalytic CO_2 formation has been reported [27]. In the following, first the experimental determination of the catalytic reaction cycle of Au_2^- will be described before results on the catalytic activity of Ag_n^- will be presented which demonstrate that also distinct silver clusters sizes show evidence to be active oxidation catalysts in the CO combustion reaction.

5.1. Au_2^-

5.1.1. Experimental reaction mechanism

As discussed above, Au_2^- reacts under conditions when solely O_2 is present in the rf-ion trap under formation of the

single product ion $Au_2O_2^-$. Analysis of the reaction kinetics depicted in Fig. 7 reveals the straight forward association reaction mechanism Eq. (1) with Au_2^- completely reacting to yield the oxide product within several seconds at room temperature. If CO is added to the ion trap, no new reaction products besides Au_2^- and $Au_2O_2^-$ are formed at $T = 300$ K as can be seen from the mass spectrum in Fig. 27a. However, surprisingly enough, Au_2^- is no longer completely transformed into oxide, but an offset appears in the gold cluster concentration at long reaction times which is apparent from the corresponding kinetics depicted in Fig. 29a. The most simple reaction mechanism that fits this data is the equilibrium reaction in which oxide is formed but bare gold dimer is reformed to a certain extend:

$$Au_2^- + O_2 \rightleftarrows Au_2O_2^-. \quad (12)$$

However, the extend to which the gold dimer is reformed increases with increasing CO concentration. Thus, the reaction mechanism must involve more intermediate steps representing the influence of CO.

To reveal the complete reaction mechanism, the reaction was investigated at lower temperatures. The product ion mass spectrum recorded at 100 K with O_2 and CO in the ion trap

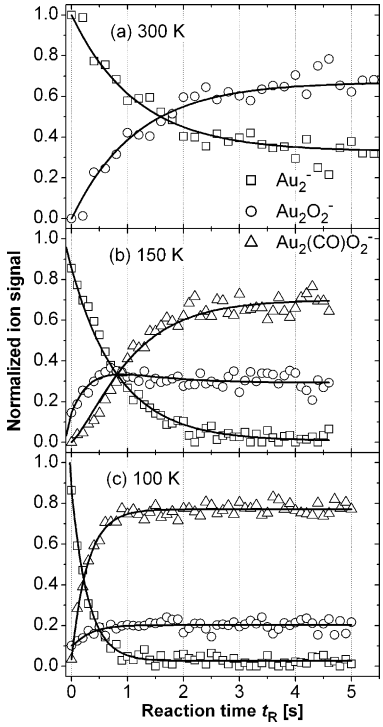

Fig. 29. Product ion concentrations as a function of the reaction time for three different reaction temperatures and different reactant gas concentrations: (a) $T = 300$ K, $p(O_2) = 0.12$ Pa, $p(CO) = 0.12$ Pa, and $p(He) = 1.2$ Pa; (b) $T = 150$ K, $p(O_2) = 0.04$ Pa, $p(CO) = 0.04$ Pa, and $p(He) = 1.0$ Pa; and (c) $T = 100$ K, $p(O_2) = 0.02$ Pa, $p(CO) = 0.03$ Pa, and $p(He) = 1.0$ Pa. Open symbols represent the normalized experimental data ((□): Au_2^-; (◯): $Au_2O_2^-$; and (△): $Au_2(CO)O_2^-$). The solid lines are obtained by fitting the integrated rate equations of the catalytic reaction cycle (Eqs. (13a)–(13c)) to the experimental data.

(Fig. 27b) shows the appearance of the coadsorption complex $Au_2(CO)O_2^-$ discussed in the preceding section. This complex represents a key intermediate in the reaction mechanism of the catalytic oxidation of CO to CO_2 as has been predicted in the earlier theoretical study [46]. The experimental evidence obtained so far demonstrates that O_2 adsorption is likely to be the first step in the observed reaction mechanism. Subsequent, CO coadsorption yields the observed intermediate (Fig. 27b) and finally the bare gold dimer ion must be reformed. The further strategy to reveal the full reaction mechanism consists in varying the available experimental parameters, i.e., reaction temperature and reactant partial pressures. This procedure leads to a series of kinetic traces similar to the one shown in Fig. 29b and c, [67]. The goal then is to find one reaction mechanism that is able to fit all experimental kinetic data obtained under the various reaction conditions. This kinetic evaluation method results in the most-simple mechanism, which is able to fit the experimental data [67]. In this way, it is possible to rule out all but one possible reaction mechanism, which is represented by the following reaction equations:

$$Au_2^- + O_2 \rightarrow Au_2O_2^- \quad (13a)$$

$$Au_2O_2^- + CO \rightleftarrows Au_2(CO)O_2^- \quad (13b)$$

$$Au_2(CO)O_2^- + CO \rightarrow Au_2^- + 2CO_2. \quad (13c)$$

The solid lines in Fig. 29 represent the fit of this mechanism to the experimental data. It equally well fits all other obtained kinetic data [67]. In this catalytic reaction cycle, $Au_2O_2^-$ reacts with CO to form $Au_2(CO)O_2^-$ which will either redissociate to the oxide or further react with a second CO molecule to reform Au_2^- while liberating two CO_2 molecules. It should be noted that the quality of the fit is very sensitive to the postulated reaction steps and that the kinetic evaluation procedure that we have employed is clearly able to discriminate against alternative mechanisms, as has been demonstrated before [36,63,64]. The replacement of the equilibrium in reaction (13b), e.g., by a simple forward reaction will lead to a mechanism that yields an inadequate fit to the experimental data. The $Au_2O_2^-$ signal will then disappear at long reaction times, which is not the case as can be seen from Fig. 29c.

5.1.2. *Adsorption sequence*

The mechanism reveals that O_2 adsorption precedes CO adsorption in the catalytic reaction. This is further supported by the fact that no signal for the ion Au_2CO^- is observed and by the reaction kinetics of Au_2^- when only O_2 or CO are present in the trap; because the adsorption of O_2 is by about an order of magnitude faster than the adsorption of CO molecules (Fig. 25) [66]. Further insight into the catalytic reaction mechanism can be obtained from partial pressure dependent measurements. The dependence of a pseudo first-order rate constant of the mechanism Eqs. (13a)–(13c) on the concentration of a reactant (O_2 or CO) demonstrates the in-

volvement of the reactant in this particular reaction step. The variation of the oxygen partial pressure inside the trap, e.g., solely affects the rate constant of reaction step (13a) and all other rate constants remain unaffected [67]. However, most interestingly, it appears that at very high CO partial pressures and low temperatures CO adsorption starts to compete with O_2 adsorption in the first reaction step. This is reflected in a systematic increase of the rate constant of reaction Eq. (13a) with increasing *p*(CO) at lower temperatures. From this side reaction, a new product $Au_2(CO)O_2^-$ with different structure than the discussed intermediate in Eqs. (13a)–(13c) will form, competing with the catalytic cycle [67].

As discussed above, the postulation of an equilibrium in step (13b) is essential to the reaction mechanism. This in turn has implications on the possible structure of the intermediate species $Au_2(CO)O_2^-$ in the catalytic cycle Eqs. (13a)–(13c) which might be a simple coadsorption of the two molecules, e.g., on different sides of Au_2^-, or already a reacted carbonate (CO_3)-like species adsorbed onto the gold dimer. Apparently, the observed intermediate can have different isomers and one of them is formed by molecular coadsorption of CO and O_2, because otherwise the possible CO loss required by Eq. (13b) would not be feasible. Therefore, several possible structures of $Au_2(CO)O_2^-$ have been calculated by Häkkinen and Landman which will be presented in the following.

5.1.3. Intermediate complex structure

Five structures corresponding to the mass of the complex $Au_2(CO)O_2^-$ were studied theoretically, and the structural and energetic information is given in Fig. 30, [67]. The formation and stability of these structures is discussed with respect to preformed $Au_2O_2^-$. This analysis leads to the conclusion that structures C and D (Fig. 30) are the ones pertinent to the observed reaction steps (13b) (equilibrium between CO association to $Au_2O_2^-$ to form Au_2 $(CO)O_2^-$ and dissociation of the latter to form $Au_2O_2^-$), and (13c) (formation of CO_2).

Structures A and B correspond to molecular coadsorption of CO and O_2 to Au_2^-. From the two molecularly coadsorbed species, CO can readily (without barrier) bind to the end of the Au–Au axis (structure A) whereas a barrier of 0.2 eV was found for CO association from the gas-phase to the Au–Au bridging site of structure B, where the Au–Au bond is significantly elongated to 3.34 Å. The barrier for forming B from A via displacement of CO from the end of the complex to the Au–Au bridge is rather high (on the order of 0.9 eV). In both structures A and B, the O–O bond is activated to a value typical to a superoxo-species (about 1.35 Å). The stability of structure C is close to that of A. It contains a reacted O–O–C–O group that is attached through the carbon atom to the gold dimer anion. The O–O bond is activated to a superoxo-state, and this species bears some resemblance to the gold–peroxyformate complex identified in the early experiments of gold atoms in cryogenic CO/O_2 matrices [48].

By far the most stable structures corresponding to the mass of $Au_2CO_3^-$ are the two carbonate species D and E [67]. Both structures were proposed by Häkkinen and Landman before [46]. Structure E requires a preformed $Au_2O_2^-$ where the molecular axes of Au_2 and O_2 lie parallel to each other. Since this structure of $Au_2O_2^-$ is 1 eV less stable than the ground state discussed above (the binding energy of oxygen in this configuration is 0.39 eV versus the optimal binding energy of 1.39 eV), it is unlikely to be formed and conse-

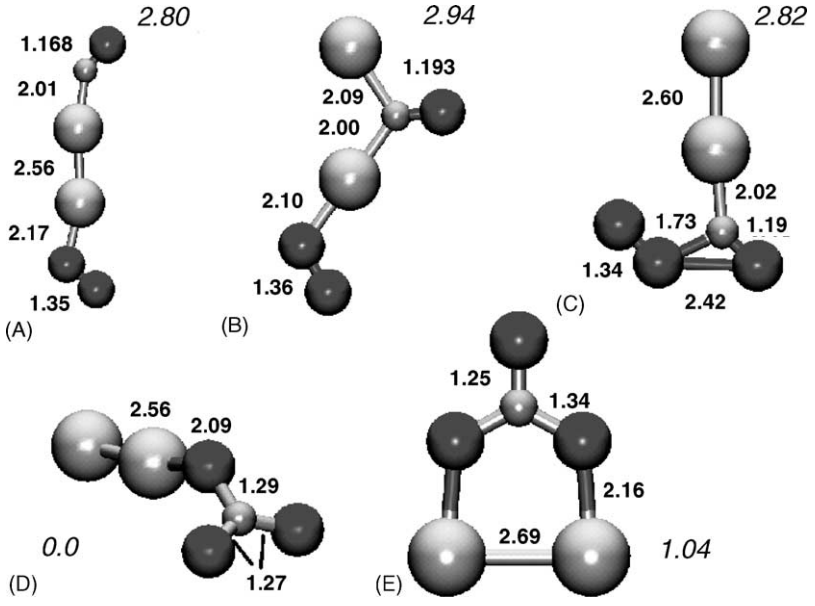

Fig. 30. Five optimized structures A–E of $Au_2(CO)O_2^-$, with bond lengths in Å. The relative stability of these structures is indicated by the numbers in italics (in eV). A, B, C, and E are planar, and the two carbonate species (D and E) have C_{2v} symmetry. Structures C and D are the ones pertinent for the reactions discussed in the text. Au atoms are depicted by large large grey spheres, a small gray sphere corresponds to the carbon atom, and the oxygen atoms are depicted by dark spheres [67].

quently structure E is not expected to play a relevant role in the catalytic cycle. On the other hand, formation of the most stable structure D by insertion of CO(g) into the O–O bond in $Au_2O_2^-$ (where the O_2 molecule is end-on bonded to the gold dimer anion) requires a barrier of only 0.3 eV, which is easily overcome under our experimental conditions.

5.1.4. Activation barriers—Eley–Rideal versus Langmuir–Hinshelwood mechanism

In Section 1.2, the general reaction mechanism of the catalytic CO oxidation reaction was presented. On an extended catalyst surface the reaction proceedes via a Langmuir–Hinshelwood-type mechanism relying fundamentally on the diffusion of the reactants on the catalyst surface. From the theoretical simulations presented in the previous section, however, it becomes apparent that a diffusion-type motion of the coadsorbed reactants on the cluster surface is not to be expected. The formation of structure C in Fig. 30, e.g., via a sequence of structures like A and B by CO motion is energetically impossible under the reaction conditions in the ion trap. Consequently, Eley–Rideal-type reaction scenarios are suggested for the formation of the proposed intermediate structures C and D (Fig. 30). Most notably, the adsorption of O_2 as well as the coadsorption of CO leading to the peroxyformate structure C are barrierless according to the calculations. The formation of the carbonate structure D requires only a small energy barrier as discussed above. This is in excellent agreement with the experimental observation that all but one step of the reaction cycle shows a negative dependence of the corresponding termolecular rate constants on the reaction temperature [67]. As discussed in Section 2.3, within the Lindemann model for low-pressure gas-phase kinetics, this negative temperature dependence is indicative of a barrierless reaction.

Only the last reaction step Eq. (13c) representing the reformation of Au_2^- and the liberation of CO_2 displays a positive temperature dependence of the rate constant [67]. This demonstrates the presence of an activation barrier in this particular reaction step. This experimental information on the reaction energetics is again in accord with theoretical modeling of the reaction pathway. Fig. 31 shows the calculated energetics along the catalytic reaction path involving the intermediate structures C (Fig. 31a) and D (Fig. 31b), respectively. In both cases, the mechanism proceeds via an ER reaction of CO(g) with the intermediate complex structures releasing two CO_2 molecules. The formation of CO_2 from the reaction between CO(g) and structure C (Fig. 31a) involves a low barrier of 0.3 eV (see the transition state configuration in Fig. 31a), resulting in the formation of a metastable $Au_2CO_2^-$ complex, where CO_2 is bound to Au_2 via the carbon atom (see the structure of this complex in Fig. 31a). However, the heat of reaction (4.75 eV) evolving from the formation of the first CO_2 molecule is large enough in order to overcome the binding energy (0.52 eV) of the remaining CO_2 to Au_2^-, thus facilitating its desorption from the metal cluster.

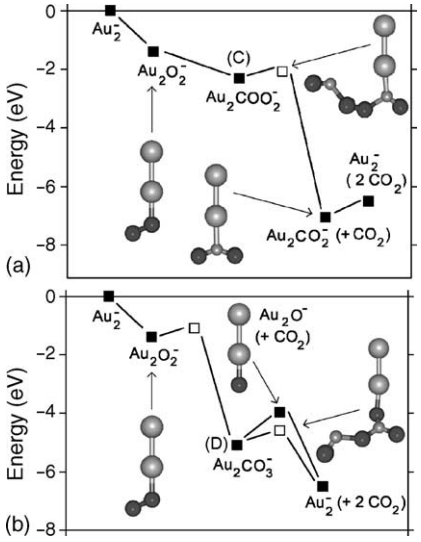

Fig. 31. The energetics of the ER mechanisms of the catalytic reaction. (a) The peroxyformate-like species $Au_2COO_2^-$ (configuration C in Fig. 30) is the metastable intermediate state. The open square denotes the reaction barrier connecting the peroxyformate-like state with the $Au_2CO_2^- + CO_2$ product, and the corresponding transition state configuration is shown at the top right. The last step of the reaction is desorption of CO_2. The initial energy level at zero corresponds to the sum of the total energies of all the reactants ($Au_2^- + O_2 + 2CO$). (b) The carbonate species $Au_2CO_3^-$ (configuration D in Fig. 30) is the metastable intermediate state. The open squares again denote the reaction barriers. The first reaction barrier is associated with the insertion of CO into the O–O bond of $Au_2O_2^-$ (see structure on the left) leading to formation of $Au_2CO_3^-$. Subsequently, two reaction paths are shown. One path involves thermal dissociation of the carbonate to produce Au_2O^- (see the structure shown at the top) which then reacts with CO(g) releasing another CO_2 molecule. The other path proceeds through an ER reaction of the carbonate with CO(g) and it results in the formation of two CO_2 molecules. The latter path involves a barrier of 0.5 eV, and the corresponding transition-state configuration is shown on the right [67].

The second scenario involves two branches (Fig. 31b) [46]. In the first one, thermal dissociation of CO_2 from the carbonate D (which is endothermic by 1.12 eV) produces a highly reactive species, Au_2O^-, which reacts spontaneously (i.e., without an activation barrier) with CO(g) to produce CO_2. The product ion Au_2O^- has, however, never been observed in the experiment. Therefore, the second branch is favored consisting of an ER reaction of CO(g) with species D to produce CO_2. While this step involves a modest barrier of 0.5 eV (denoted by an open square, with the corresponding transition-state configuration shown on the right in Fig. 31b), it releases readily two CO_2 molecules, since the remaining $Au_2CO_2^-$ species, where CO_2 is bound to Au_2 via one of the oxygen atoms, is unstable under our experimental conditions (100–300 K) [67].

The detailed catalytic reaction cycle emerging from experimental and theoretical evidence for the CO oxidation by gas-phase Au_2^- clusters is depicted in Fig. 32. Also included are the calculated energy barriers for the different reaction steps and the simulated intermediate structures. In addition to a comprehensive molecular mechanistic understanding based on experiment and theory, the efficiency of the catalytic re-

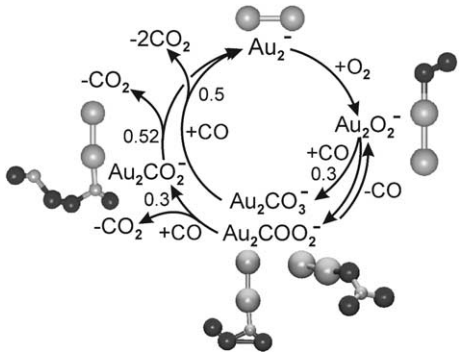

Fig. 32. Schematic representation of the gas-phase catalytic cycle for the oxidation of carbon monoxide by gold dimer anions, based on the reaction mechanism determined by kinetic measurements in conjunction with first-principles simulations. The numbers denote calculated energy barriers (in eV). Also displayed are geometrical structures of reactants and intermediate products according to the calculations (large grey spheres: Au; small grey spheres: C; dark spheres: O) [67].

action can be estimated from the experimental kinetic data as presented in the following section.

5.1.5. Catalytic turn-over-frequency (TOF)

From the kinetic fit, it is possible to simulate the CO_2 formation rate, and thus to obtain the turn-over-frequency of the catalytic reaction. The simulated CO_2-yield under the reaction conditions of Fig. 29a is displayed in Fig. 33. The corresponding TOF amounts to 0.4 CO_2 molecules per gold cluster per second. For the conditions of Fig. 29c, a TOF of 0.3 CO_2 molecules per gold cluster per second was estimated. These values are in the same order of magnitude as the catalytic activity of oxide supported gold cluster particles with a size of a few nanometers, which ranges between 0.2 s^{-1} per Au atom (~2 nm diameter particles at 273 K) and 4 s^{-1} per Au atom (3.5 nm particles at 350 K) [6].

In order to approach an understanding of the deduced TOFs in the gas-phase reactor experiment, a rough estimation of the number of collisions of a metal cluster with the required reactant molecules (O_2 and 2 CO) in the trap will be given [95]. The collision frequency in the trap is about 10^5 s^{-1} [36]. The reactant gas concentrations are about 10% or less

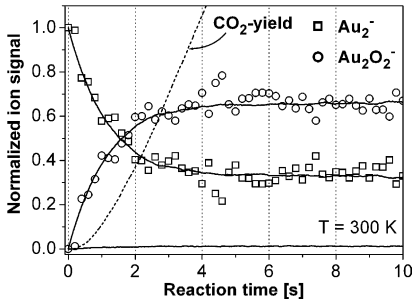

Fig. 33. Simulated CO_2 formation (dashed line) for the experimental conditions of Fig. 29b. The CO_2 concentration increases exponentially with time until the Au_2^- and $Au_2O_2^-$ signals reach equilibrium. The rise then remains linear and from the corresponding slope the TOF is estimated [95].

of the helium concentration. Hence, ~100 collisions per second of an Au_2^- ion might potentially lead to the catalytic formation of one CO_2 molecule. Considering the measured TOFs, a reaction efficiency (successful versus total number of collisions) of 0.3–0.5% depending on the exact reaction conditions can be estimated. Baring in mind that the gas-phase catalytic reaction proceed via an Eley–Rideal mechanism in which the reactant molecule must collide in exactly the right location with exactly the correct orientation in order for the reaction to proceed, an efficiency of about 1% of all collisions leading to CO_2 formation can be considered surprisingly large. This indicates that the TOF in the ion trap reactor experiment is mainly limited by the collision frequency, i.e., the reactant partial pressures. These considerations also confirm the high efficiency of catalytic gas-phase clusters ion reactions previously observed by Ervin and co-workers [57].

5.2. Ag_n^-

5.2.1. Reactive oxide complexes $Ag_nO_4^-$

As the final example, the potential catalytic activity of small silver cluster anions in the CO oxidation reaction under the conditions of our ion trap reactor experiment will be discussed. As explained above, O_2 is more strongly bound to Ag_2^- than to Au_2^- (cf. Section 4.1.4), which makes it unlikely for the catalytic CO oxidation on Ag_2^- to proceed under thermal reaction conditions. In addition, no reaction of any Ag_n^- cluster size with CO is observed. However, although the odd size Ag^- and Ag_3^- only react very poorly with a first O_2, as can be seen from Fig. 18, they eagerly adsorb a second oxygen molecule to form $Ag_nO_4^-$ (odd n) complexes [33]. Theoretical calculations predict that this second oxygen molecule is differently bound to the silver cluster anion with the O_2 bond elongated in a superoxo-like subunit, which is activated for further oxidation reactions (see Section 4.1.3). Indeed, very size selective reactions of these $Ag_nO_4^-$ could be confirmed experimentally [40]. No reactions for the smallest cluster sizes with $n = 1$ and 3 have been observed, but already for the case of Ag_5^-, the reaction of CO with the $Ag_5O_4^-$ complex is apparent from the product ion mass spectrum shown in Fig. 34. Also displayed in Fig. 34 is the calculated structure of the complex with the activated second oxygen molecule in a doubly bound bridging position [33]. No coadsorption of CO and O_2 onto Ag_5^- was observed, but the formation of the fragment ion $Ag_3CO_2^-$ points toward a reaction between CO and O_2 involved with the metal cluster decomposition. The observed strong fragmentation is probably due to the fact that the small cluster is not able to accommodate the excess energy liberated in the formation of the intermediate energized complex, which then is likely to decompose.

5.2.2. Strongly size dependent reaction of Ag_n^- with O_2 and CO

For the larger sizes Ag_n^- ($n = 7$–13), the most surprising behavior was observed: filling the trap with CO in addition to

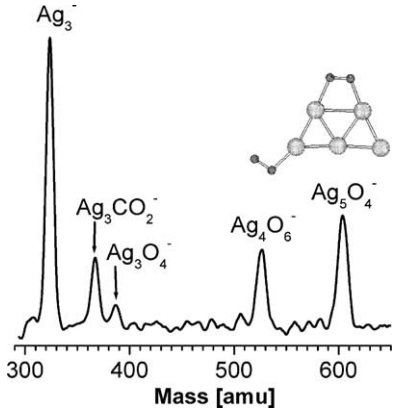

Fig. 34. Product ion mass spectrum after reaction of Ag_5^- with O_2 and CO. Reaction conditions: $T = 100$ K, $p(O_2) = 0.01$ Pa, $p(CO) = 0.03$ Pa, $p(He) = 1.23$ Pa, and $t_R = 1$ s. The calculated structure of $Ag_5O_4^-$ is indicated [33]. This complex is formed first and than further reacts with CO [40].

O_2 resulted in a partial reduction or even a complete depletion of $Ag_nO_4^-$ signals and a corresponding increase of the bare Ag_n^- cluster signals for odd n, while the $Ag_nO_2^-$ peaks (n even) and Ag_{13}^- remained unaffected by CO addition. Fig. 35 shows the corresponding product ion mass spectra at 100 K and equal reaction times, but under different reaction conditions: (a) when only trace amounts of oxygen are present in the trap, odd size clusters Ag_7^-, Ag_9^-, and Ag_{13}^- do not react, Ag_{11}^- yields some product $Ag_{11}O_4^-$, while even size clusters completely react to $Ag_nO_2^-$ products. (b) When the oxygen partial pressure is raised to 0.01 Pa, Ag_7^- reacts and forms the oxide $Ag_7O_4^-$, Ag_9^- almost completely disappears and the products $Ag_9O_2^-$, and $Ag_9O_4^-$ are observed, also the Ag_{11}^- signal almost vanishes, and $Ag_{11}O_4^-$ remains. The product ion mass spectrum (c) was obtained under conditions where partial pressures of both reactants, O_2 and CO, are present in the trap. Unexpectedly, the bare silver cluster signals Ag_9^- and Ag_{11}^- reappear, while the corresponding oxide product intensities decrease considerably. Also in the case of Ag_7^-, the bare to oxide cluster ratio shifts in favor of the bare Ag_7^-. This pronounced signal enhancement of the bare metal clusters cannot be explained by fragmentation of larger clusters, because signal intensities are much weaker for the larger cluster sizes (cf. Fig. 35).

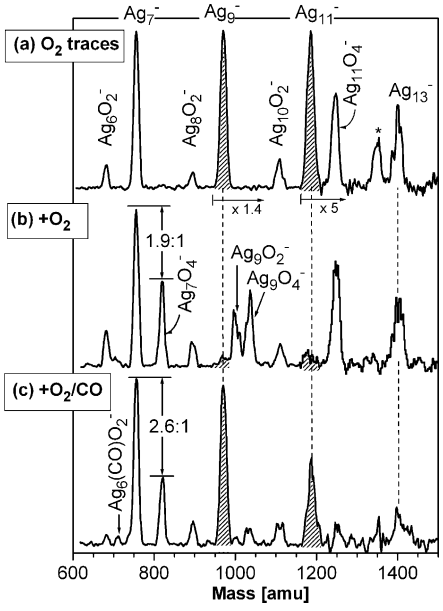

Fig. 35. Product ion mass spectra of silver clusters Ag_{7-13}^- obtained at $T = 100$ K and $t_R = 0.1$ s with different reactant concentrations in the ion trap. (a) Reaction with trace amounts of oxygen ($p_{He} = 1.2$ Pa), (b) reaction with oxygen ($p(O_2) = 0.01$ Pa and $p(He) = 1.17$ Pa), and (c) reaction with oxygen and carbon monoxide ($p(O_2 = 0.01$ Pa, $p(CO) = 0.03$ Pa, and $p(He) = 1.17$ Pa). In the case of Ag_7^-, the bare to oxide cluster signal ratio is indicated in (b) and (c). The Ag_9^- and Ag_{11}^- mass peaks (hatched) disappear almost completely after reaction with oxygen and reappear when CO is added. The peak in (a) labeled by an asterix would correspond to the mass of $Ag_{12}O_4^-$, but is only observed at extremely low oxygen partial pressures (traces) and does not appear at measurable O_2 content [40].

Considering the fact that the pure metal clusters do not react with carbon monoxide, the conclusion can be drawn that CO reacts with the oxides of Ag_7^-, Ag_9^-, and Ag_{11}^-. The observed complexes $Ag_nO_4^-$ are then the decisive intermediates in the reaction with CO. The present data thus provide evidence that, in contrast to other cluster sizes, silver cluster anions with $n = 7$, 9, and 11 activate the adsorbed oxygen to be able to react with CO under our reaction conditions. In this process, CO_2 is likely to be liberated and the metal clusters are reformed to complete a catalytic reaction cycle.

6. Conclusions and outlook

For the gas-phase ion chemistry of small noble metal clusters of silver and gold, the statement that “each atom counts” [4,5,116] is particularly true, because changes in chemical reactivity over orders of magnitude are observed when the cluster size changes by a single atom. However, not only the cluster size is an important parameter for the reactive behavior of these clusters, but also the charge state. Therefore, the above statement might be extended accordingly by “each electron counts as well”. In the case of small silver clusters, it could be demonstrated that dioxygen adsorbs molecularly on the negatively charged clusters, whereas dissociative atomic adsorption is observed for Ag_2^+. In this example, the essential requirement of precise reaction temperature control becomes apparent because the cleavage of the oxygen bond on Ag_2^+ is an activated process and strongly temperature dependent. The experimental control of the reaction temperature is one major advantage of the rf-ion trap technique presented in this contribution. It not only provides defined, reproducible reaction conditions, but also enables the determination of the reaction energetic through temperature dependent kinetic measurements. This is particularly valuable for the comparison with first principles simulations as could be demonstrated for the catalytic CO oxidation cycle on Au_2^-.

Apart from the cluster electronic and geometric structure, each atom counts also for the capability of the cluster to accommodate excess reaction energy in the cluster-complex microcanonical system, in particular in the very small size range. This could be demonstrated through kinetic measurements of the reaction of small gold cluster anions with CO. The cluster reactivity also strongly depends on the exact chemical composition. In several recent contributions, the strong influence of relativistic effects on the bonding in gold clusters and on their reactivity was emphasized [77,79,81]. Our ion trap measurements confirm the influence of relativistic level structure changes on the cluster reaction rates leading unexpectedly to the non-reactivity of binary silver–gold trimer anions toward both O_2 and CO.

A further important issue emphasized in this contribution is the influence of an adsorbate molecule, O_2 or CO, on the electronic and geometric structure of the metal cluster complex. Such adsorbate induced alternations of the cluster complex structure become apparent when the reactivity toward a second adsorbate molecule is very different from that of the bare metal clusters. It could be demonstrated that in the case of silver and gold cluster anions, this effect often leads to a cooperative action and results in coadsorption complexes which could be identified in several cases to be decisive intermediates of catalytic reactions. For the case of Au_2^-, the ion trap kinetic measurements in combination with first principles simulations lead to the discovery of the catalytic activity of this particular ion and provide a comprehensive molecular picture of the reaction mechanism and energetics [46,67].

A particularly appealing experimental advantage of rf-ion trap technique consists in the use of the trap as a gas-phase catalytic reactor as proposed previously by Ervin [3]. The metal cluster ions can be stored inside the trap while reactant gases flow through and are converted into desired products. In this way, from the kinetic evaluation, the catalytic turn-over-frequency can be estimated and compared, e.g., to supported cluster catalyst materials.

Future prospects of the presented ion trap technique in application to catalytic reactions of noble metal clusters are manifold. With respect to the metal cluster ions, one major aim is the investigation of larger cluster sizes to eventually approach the bulk limit where, e.g., the influence of the charge state on the interaction of O_2 with silver clusters is expected to become negligible. With respect to the CO oxidation reaction, one widely open issue of major importance is the influence of humidity on the catalytic reaction behavior [117]. We think that the ion trap technique provides an excellent tool to study the influence of water molecule by molecule. Of course, it is also planned to extend the ion trap investigations to other important noble metal catalyzed chemical reactions such as, e.g., the selective oxidation of ethylene or of propylene [118]. Our laboratory also provides the opportunity to apply laser spectroscopic techniques to the cluster complexes stored inside the ion trap [110] to provide an even more detailed molecular picture of, e.g., the intermediate coadsorption complexes. In particular, the probing of the molecular catalytic reaction dynamics by ultra-fast laser spectroscopy is one major goal and the viability of this experimental scheme has been demonstrated recently [119]. Finally, the combination of ion trap reaction kinetics and ultra-fast laser techniques might eventually not only lead to the observation of catalytic metal cluster reactions in real time, but also possibly to the selective control of catalytic reactions by tailored ultra-fast laser pulses [120].

Acknowledgements

I am most grateful to Professor Ludger Wöste for his strong support of the research work described in the present paper. His enthusiasm and his passion for the world of small metal clusters is tremendously motivating. The fruitful and most helpful collaboration with Professor Ueli Heiz is gratefully acknowledged. The experimental results described in this review were obtained as a part of the Ph.D. thesis's of Dr. Liana D. Socaciu-Siebert and Dr. Jan Hagen. I am very grateful for their significant contributions. I am also greatly indebted to the Diploma and Master students Maryam Elijazyfer, Denisia M. Popolan, and Mihai Vaida for their contributions and help. Experimental support from Dr. Jérôme Le Roux and Dr. Štefan Vajda is also gratefully acknowledged. Furthermore, I would like to thank Dr. Hannu Häkkinen and Professor Uzi Landman for theoretical support and fruitful discussions concerning the gold cluster experiments. In the case of the silver cluster reactions, support and helpful discussions with Professor Vlasta Bonačić-Koutecký, Dr. Roland Mitrić, and Holger Noack are acknowledged. I also thank Dr. Bert Stegemann and Dr. Roland Mitrić for critical reading of the manuscript. Finally, the financial support by the Deutsche Forschungsgemeinschaft is gratefully acknowledged.

References

[1] A. Kaldor, D.M. Cox, M.R. Zakin, Adv. Chem. Phys. 70 (1988) 211;
M.B. Knickelbein, Annu. Rev. Phys. Chem. 50 (1999) 79.
[2] D.C. Parent, S.L. Anderson, Chem. Rev. 92 (1992) 1541.
[3] K.M. Ervin, Int. Rev. Phys. Chem. 20 (2001) 127.
[4] V. Bonačić-Koutecký, P. Fantucci, J. Koutecký, Chem. Rev. 91 (1991) 1035;
J. Jortner, Z. Phys. D 24 (1992) 247.
[5] U. Landman, Int. J. Mod. Phys. B 6 (1992) 3623.
[6] M. Haruta, Catal. Today 36 (1997) 153;
M. Haruta, M. Daté, Appl. Catal. A 222 (2001) 427;
M. Valden, X. Lai, D.W. Goodman, Science 281 (1998) 1647.
[7] G.C. Bond, D.T. Thompson, Catal. Rev. Sci. Eng. 41 (1999) 319;
P.H. Abelson, Science 288 (2000) 269;
R. Meyer, C. Lemire, S.K. Shaikhutdinov, H.-J. Freund, Gold Bull. 37 (2004) 72.
[8] B. Hammer, J.K. Nørskov, Nature 376 (1995) 238.
[9] A. Sanchez, S. Abbet, U. Heiz, W.-D. Schneider, H. Häkkinen, R.N. Barnett, U. Landmann, J. Phys. Chem. A 103 (1999) 9573.
[10] T.E. Lefort, French patents, Societé Francaise de Catalyse Generalisee. France: FR 729925, 1931, and FR 739562, 1931.

[11] B.C. Gates, Catalytic Chemistry, John Wiley & Sons Inc., New York, Singapore, 1992.
[12] R.J. Madix, J.T. Roberts, in: R.J. Madix (Ed.), Surface Reactions, Springer-Verlag, Berlin, 1994.
[13] D.M. Cox, R.O. Brickman, K. Creegan, A. Kaldor, Mat. Res. Soc. Symp. Proc. 206 (1991) 43.
[14] L.D. Socaciu-Siebert, Dissertation, Freie Universität Berlin, Berlin, 2004.
[15] K. Koszinowski, D. Schröder, H. Schwarz, Chem. Phys. Chem. 4 (2003) 1233;
M.L. Kimble, A.W. Castleman Jr., Int. J. Mass Spectrom. 233 (2004) 99.
[16] D.M. Cox, R. Brickman, K. Creegan, A. Kaldor, Z. Phys. D 19 (1991) 353.
[17] T.H. Lee, K.M. Ervin, J. Phys. Chem. 98 (1994) 10023.
[18] B.E. Salisbury, W.T. Wallace, R.L. Whetten, Chem. Phys. 262 (2000) 131.
[19] C. Jackschath, I. Rabin, W. Schulze, Ber. Bunsenges. Phys. Chem. 96 (1992) 1200.
[20] J. Ho, K.M. Ervin, W.C. Lineberger, J. Chem. Phys. 93 (1990) 6987.
[21] K.J. Taylor, C.L. Pettiette-Hall, O. Cheshnovsky, R.E. Smalley, J. Chem. Phys. 96 (1992) 3319.
[22] H. Handschuh, G. Ganteför, P.S. Bechthold, W. Eberhardt, J. Chem. Phys. 100 (1994) 7093.
[23] J. Hagen, L.D. Socaciu, M. Elijazyfer, U. Heiz, T.M. Bernhardt, L. Wöste, Phys. Chem. Chem. Phys. 4 (2002) 1707.
[24] M.A. Nygren, P.E.M. Siegahn, C. Jin, T. Guo, R.E. Smalley, J. Chem. Phys. 95 (1991) 6181.
[25] W.T. Wallace, R.L. Whetten, J. Phys. Chem. B 104 (2000) 10964.
[26] W.T. Wallace, R.L. Whetten, Eur. J. Phys. D 16 (2001) 123;
I. Balteanu, O.P. Balaj, B.S. Fox, M.K. Beyer, Z. Bastl, V.E. Bondybey, Phys. Chem. Chem. Phys. 5 (2003) 1213.
[27] W.T. Wallace, R.L. Whetten, J. Am. Chem. Soc. 124 (2002) 7499.
[28] P. Fayet, L. Wöste, Surf. Sci. 156 (1985) 135.
[29] W. Andreoni, T.H. Upton, J.L. Marins, Helv. Phys. Acta 58 (1985) 816;
K. Laihing, P.Y. Cheng, M.A. Duncan, Z. Phys. D 13 (1989) 161;
V.A. Spasov, T.H. Lee, J.P. Maberry, K.M. Ervin, J. Chem. Phys. 110 (1999) 5208;
S. Krückenberg, G. Dietrich, K. Lützenkirchen, L. Schweikhard, C. Walther, J. Ziegler, Eur. J. Phys. D 9 (1999) 169;
S. Srinivas, U.A. Salian, J. Jellinek, in: N. Russo, D.R. Salahub (Eds.), Metal-Ligand interactions in Biology, Chemistry and Physics, Kluwer Academic Publishers, Dordrecht, 2000;
J. Zhao, Y. Luo, G. Wang, Eur. J. Phys. D 3 (2001) 309;
R. Fournier, J. Chem. Phys. 115 (2001) 2165;
M.N. Huda, A.K. Ray, Phys. Rev. A 67 (2003) 013201.
[30] G. Ganteför, M. Gausa, K.H. Meiwes-Broer, H.O. Lutz, J. Chem. Soc. Faraday Trans. 86 (1990) 2483;
H. Handschuh, C.-Y. Cha, P.S. Bechthold, G. Ganteför, W. Eberhardt, J. Chem. Phys. 102 (1995) 6406.
[31] V. Bonačić-Koutecký, L. Cespiva, P. Fantucci, J. Pittner, J. Koutecký, J. Chem. Phys. 100 (1994) 490.
[32] S. Wolf, G. Sommerer, S. Rutz, E. Schreiber, T. Leisner, L. Wöste, R.S. Berry, Phys. Rev. Lett. 74 (1995) 4177.
[33] J. Hagen, L.D. Socaciu, J. Le Roux, D. Popolan, T.M. Bernhardt, L. Wöste, R. Mitrić, H. Noack, V. Bonačić-Koutecký, J. Am. Chem. Soc. 126 (2004) 3442.
[34] L. Lian, P.A. Hackett, D.M. Rayner, J. Chem. Phys. 99 (1993) 2583.
[35] C. Bréchignac, P. Cahuzac, J. Leygnier, I. Tignères, Chem. Phys. Lett. 303 (1999) 304.
[36] L.D. Socaciu, J. Hagen, U. Heiz, T.M. Bernhardt, T. Leisner, L. Wöste, Chem. Phys. Lett. 340 (2001) 282.
[37] M.J. Manard, P.R. Kemper, M.T. Bowers, Int. J. Mass Spectrom. 228 (2003) 865.
[38] M. Schmidt, P. Cahuzac, C. Bréchignac, H.-P. Cheng, J. Chem. Phys. 118 (2003) 10956.
[39] M. Schmidt, A. Masson, C. Bréchignac, Phys. Rev. Lett. 91 (2003) 243401.
[40] L.D. Socaciu, J. Hagen, J. Le Roux, D. Popolan, T.M. Bernhardt, L. Wöste, S. Vajda, J. Chem. Phys. 120 (2004) 2078.
[41] K. Christmann, Introduction to Surface Physical Chemistry, Topics in Physical Chemistry, Springer Verlag, Berlin, 1991.
[42] G.A. Somorjai, Introduction to Surface Chemistry and Catalysis, John Wiley & Sons Inc., New York, 1994.
[43] A.F. Hollemann, N. Wiberg, Lehrbuch der Anorganischen Chemie, Walter de Gruyter, Berlin, 1995.
[44] H. Conrad, G. Ertl, J. Küppers, Surf. Sci. 76 (1978) 323.
[45] G. Ertl, in: J.R. Anderson, M. Boudart (Eds.), Catalysis, Science and Technology, Springer, Berlin, 1983.
[46] H. Häkkinen, U. Landman, J. Am. Chem. Soc. 123 (2001) 9704.
[47] J.R. Hahn, W. Ho, Phys. Rev. Lett. 87 (2001) 166102.
[48] H. Huber, D. McIntosh, G.A. Ozin, Inorg. Chem. 16 (1977) 975.
[49] D. Stolcic, M. Fischer, G. Ganteför, Y.D. Kim, Q. Sun, P. Jena, J. Am. Chem. Soc. 125 (2003) 2848.
[50] Y.D. Kim, M. Fischer, G. Ganteför, Chem. Phys. Lett. 377 (2003) 170.
[51] Y.D. Kim, Int. J. Mass Spectrom. 238 (2004) 17.
[52] Q. Sun, P. Jena, Y.D. Kim, M. Fischer, G. Ganteför, J. Chem. Phys. 120 (2004) 6510.
[53] Y.D. Kim, G. Ganteför, Chem. Phys. Lett. 383 (2004) 80.
[54] M.M. Kappes, R.H. Staley, J. Am. Chem. Soc. 103 (1981) 1286;
C. Berg, S. Kaiser, T. Schindler, C. Kronseder, G. Niedner-Schattenburg, V.E. Bondybey, Chem. Phys. Lett. 231 (1994) 139;
R. Wesendrup, H. Schwarz, Organometallics 16 (1997) 461;
M. Pavlov, M.R.A. Blomberg, P.E.M. Siegbahn, R. Wesendrup, C. Heinemann, H. Schwarz, J. Phys. Chem. A 101 (1997) 1567;
M. Bronstrup, D. Schroder, I. Kretzschmar, H. Schwarz, J.N. Harvey, J. Am. Chem. Soc. 123 (2001) 142;
M.R. Sievers, P.B. Armentrout, Int. J. Mass Spectrom. 185-187 (1999) 117;
T. Waters, R.A.J. O'Hair, A.G. Wedd, J. Am. Chem. Soc. 125 (2003) 3384;
V. Blagojevic, M.J.Y. Jarvis, E. Flaim, G.K. Koyanagi, V.V. Lavrov, D.K. Böhme, Angew. Chem. Int. Ed. 42 (2003) 4923.
[55] R.A.J. O'Hair, G.N. Khairallah, J. Clust. Sci. 15 (2004) 331;
D.K. Böhme, H. Schwarz, Angew. Chem. Int. Ed. (2005), in press.
[56] P. Schnabel, K.G. Weil, M.P. Irion, Angew. Chem. Int. Ed. Engl. 31 (1992) 636.
[57] Y. Shi, K.M. Ervin, J. Chem. Phys. 108 (1998) 1757.
[58] D. Gerlich, in: C.-Y. Ng, M. Baer (Eds.), State-Selected and State-to-State Ion–molecule Reaction Dynamics. Part 1. Experiment, John Wiley & Sons Inc., New York, 1992.
[59] R. Keller, F. Nöhmeier, P. Spädtke, M.H. Schönenberg, Vacuum 34 (1984) 31.
[60] H. Hess, S. Kwiet, L. Socaciu, S. Wolf, T. Leisner, L. Wöste, Appl. Phys. B 71 (2000) 337.
[61] D.A. Dahl, SIMION 3D Version 7.0, EG&G Idaho Inc., 2000.
[62] J. Westergren, H. Grönbeck, S.-G. Kim, D. Tománek, J. Chem. Phys. 107 (1997) 3071;
J. Westergren, H. Grönbeck, A. Rosén, S. Nordholm, J. Chem. Phys. 109 (1998) 9848.
[63] J.I. Steinfeld, J.S. Francisco, W.L. Hase, Chemical Kinetics and Dynamics, Prentice Hall, Upper Saddle River, NJ, 1999.
[64] K.J. Laidler, Chemical Kinetics, HarperCollins, New York, 1987.
[65] E. Schumacher, DETMECH – Chemical Reaction Kinetics Software, University of Bern: Chemistry Department, 1997;
IBM – Chemical Kinetics Simulator, first ed., IBM Corporation, 1995.

[66] J. Hagen, L.D. Socaciu, U. Heiz, T.M. Bernhardt, L. Wöste, Eur. J. Phys. D 24 (2003) 327.
[67] L.D. Socaciu, J. Hagen, T.M. Bernhardt, L. Wöste, U. Heiz, H. Häkkinen, U. Landman, J. Am. Chem. Soc. 125 (2003) 10437.
[68] A.W. Castleman Jr., K.G. Weil, S.W. Sigsworth, R.E. Leuchtner, R.G. Keesee, J. Chem. Phys. 86 (1987) 3829.
[69] G. Gioumousis, D.P. Stevenson, J. Chem. Phys. 29 (1958) 294.
[70] T.M. Bernhardt, D. Popolan, L.D. Socaciu-Siebert, J. Hagen, M. Vaida, J. Le Roux, L. Wöste, Eur. J. Phys. D, in preparation.
[71] L.D. Socaciu-Siebert, J. Hagen, T.M. Bernhardt, L. Wöste, J. Phys. Chem. A, in preparation.
[72] H. Häkkinen, B. Yoon, U. Landman, X.L. Li, H.-J. Zahi, L.-S. Wang, J. Phys. Chem. A 107 (2003) 6168.
[73] Y. Negeshi, Y. Nakamura, A. Nakajima, K. Kaya, J. Chem. Phys. 115 (2001) 3657.
[74] G.F. Ganteför, D.M. Cox, A. Kaldor, J. Chem. Phys. 93 (1990) 8395;
G.F. Ganteför, D.M. Cox, A. Kaldor, J. Chem. Phys. 94 (1991) 854;
G.F. Ganteför, D.M. Cox, A. Kaldor, J. Chem. Phys. 96 (1992) 4102.
[75] K.J. Taylor, C. Jin, J. Conceicao, L.-S. Wang, O. Cheshnovsky, B.R. Johnson, P.J. Nordlander, R.E. Smalley, J. Chem. Phys. 93 (1990) 7515.
[76] M. Niemietz, P. Gerhardt, G. Ganteför, Y.D. Kim, Chem. Phys. Lett. 380 (2003) 99.
[77] K. Balasubramanian, Relativistic Effects in Chemistry, Wiley and Sons, New York, 1997.
[78] S.C. Fain, J.M. McDavid, Phys. Rev. B 9 (1974) 5099.
[79] H. Schwarz, Angew. Chem. Int. Ed. 42 (2003) 4442.
[80] P. Pyykkö, Chem. Rev. 88 (1988) 563.
[81] H. Häkkinen, M. Moseler, U. Landman, Phys. Rev. Lett. 89 (2002) 033401.
[82] H.M. Lee, M. Ge, B.R. Sahu, P. Tarakeshwar, K.S. Kim, J. Phys. Chem. B 107 (2003) 9994.
[83] F. Furche, R. Ahlrichs, P. Weis, C. Jacob, S. Gilb, T. Bierweiler, M.M. Kappes, J. Chem. Phys. 117 (2002) 6982.
[84] V. Bonačić-Koutecký, V. Veyret, R. Mitrić, J. Chem. Phys. 115 (2001) 10450.
[85] V. Bonacic-Koutecky, J. Burda, R. Mitrić, M. Ge, G. Zampella, P. Fantucci, J. Chem. Phys. 117 (2002) 3120.
[86] S. Gilb, P. Weis, F. Furche, R. Ahlrichs, M.M. Kappes, J. Chem. Phys. 116 (2002) 4094.
[87] M. Okumura, Y. Kitagawa, M. Haruta, K. Yamaguchi, Chem. Phys. Lett. 346 (2001) 163;
Wells et al., 2002 D.H. Wells, W.N. Delgass, T.T. Kendall, J. Chem. Phys. 117 (2002) 10597;
Lopez and Nørskov, 2002 N. Lopez, J.K. Nørskov, J. Am. Chem. Soc. 124 (2002);
R. Mitrić, C. Bürgel, J. Burda, V. Bonačić-Koutecký, P. Fantucci, Eur. J. Phys. D 24 (2003) 41;
B. Yoon, H. Häkkinen, U. Landman, J. Phys. Chem. A 107 (2003) 4066;
M.L. Kimble, A.W. Castleman Jr., R. Mitrić, C. Bürgel, V. Bonačić-Koutecký, J. Am. Chem. Soc. 126 (2004) 2526.
[88] G. Mills, M.S. Gordon, H. Metiu, Chem. Phys. Lett. 359 (2002) 493.
[89] D.W. Yuan, Z. Zeng, J. Chem. Phys. 120 (2004) 6574.
[90] V. Bonačić-Koutecký, M. Boiron, J. Pittner, P. Fantucci, J. Koutecký, Eur. Phys. J. D 9 (1999) 183.
[91] Y.-M. Chen, P.B. Armentrout, J. Chem. Phys. 103 (1995) 618.
[92] F. Besenbacher, J.K. Nørskov, Progr. Surf. Sci. 44 (1993) 5.
[93] D. Andrae, U. Haeussermann, M. Dolg, H. Stoll, H. Preuss, Theor. Chim. Acta 77 (1990) 123;
A.D. Becke, J. Chem. Phys. 98 (1988) 5648.
[94] W.T. Wallace, R.B. Wyrwas, R.L. Whetten, R. Mitrić, V. Bonačić-Koutecký, J. Am. Chem. Soc. 125 (2003) 8408.
[95] T.M. Bernhardt, L.D. Socaciu-Siebert, J. Hagen, L. Wöste, Appl. Catal. A, submitted for publication.
[96] C. Elschenbroich, A. Salzer, Organometallics, VCH, Weinheim, 1989.
[97] H. Huber, P. Kündig, M. Moskovits, G.A. Ozin, J. Am. Chem. Soc. 97 (1975) 2097;
D. McIntosh, G.A. Ozin, J. Am. Chem. Soc. 98 (1976) 3167;
D. McIntosh, G.A. Ozin, Inorg. Chem. 16 (1977) 51.
[98] V. Bonačić-Koutecký, L. Cespiva, P. Fantucci, J. Koutecký, J. Chem. Phys. 98 (1993) 7981;
H. Häkkinen, U. Landman, Phys. Rev. B 62 (2000) R2287.
[99] X. Wu, L. Senapati, S.K. Nayak, A. Selloni, M. Hajaligol, J. Chem. Phys. 117 (2002) 4010.
[100] B. Liang, L. Andrews, J. Phys. Chem. A 104 (2000) 9156.
[101] M. Zhou, L. Andrews, C.W. Bauschlicher Jr., Chem. Rev. 101 (20011931).
[102] P.H. Kasai, P.M. Jones, J. Am. Chem. Soc. 107 (1985) 6385.
[103] J. Hagen, Dissertation, Freie Universität Berlin, Berlin, 2004.
[104] F. Meyer, Y.-M. Chen, P.B. Armentrout, J. Am. Chem. Soc. 117 (1995) 4071.
[105] G. Lüttgens, N. Pontius, P.S. Bechthold, M. Neeb, W. Eberhardt, Phys. Rev. Lett. 88 (2002) 076102.
[106] R.E. Leuchtner, A.C. Harms, A.W. Castleman Jr., J. Chem. Phys. 92 (1990) 6527.
[107] D.M. Cox, K.C. Reichmann, D.J. Trevor, A. Kaldor, J. Chem. Phys. 88 (1988) 111.
[108] V. Bonačić-Koutecký, private communication;
Phala et al., 2004 N.S. Phala, G. Klatt, E. van Steen, Chem. Phys. Lett. 395 (2004) 33.
[109] C. Ruggiero, P. Hollins, J. Chem. Soc., Faraday Trans. 92 (1996) 4829.
[110] T.M. Bernhardt, J. Hagen, L.D. Socaciu-Siebert, R. Mitrić, A. Heidenreich, J. Le Roux, D. Popolan, M. Vaida, L. Wöste, V. Bonačić-Koutecký, J. Jortner, Chem. Phys. Chem., in press.
[111] G. McElhiney, H. Papp, J. Pritchard, Surf. Sci. 54 (1976) 617;
G. Doyen, G. Ertl, Surf. Sci. 60 (1977) 397.
[112] G. McElhiney, J. Pritchard, Surf. Sci. 60 (1976) 397;
M.L. Kottke, R.G. Greenler, H.G. Tompkins, Surf. Sci. 32 (1972) 231.
[113] K. Koszinowski, D. Schroder, H. Schwarz, J. Am. Chem. Soc. 125 (2003) 3676.
[114] T. Leisner, S. Vajda, S. Wolf, L. Wöste, R.S. Berry, J. Chem. Phys. 111 (1999) 1017.
[115] W. Wallace, A.J. Leavitt, R.L. Whetten, Chem. Phys. Lett. 368 (2003) 774;
S.A. Varganov, R.M. Olson, M.S. Gordon, G. Mills, H. Metiu, Chem. Phys. Lett. 368 (2003) 778.
[116] U. Heiz, A. Sanchez, S. Abbet, W.-D. Schneider, J. Am. Chem. Soc. 121 (1999) 3214.
[117] M. Daté, M. Okumura, S. Tsubota, M. Haruta, Angew. Chem. Int. Ed. 43 (2004) 2129.
[118] C. Qi, T. Akita, M. Okumura, M. Haruta, Appl. Catal. A 218 (2001) 81.
[119] L.D. Socaciu-Siebert, J. Hagen, D. Popolan, J. Le Roux, S. Vajda, T.M. Bernhardt, L. Wöste, Eur. Phys. Chem. Chem. Phys., in preparation.
[120] C. Daniel, J. Full, L. Gonzalez, C. Lupulescu, J. Manz, A. Merli, S. Vajda, L. Wöste, Science 299 (2003) 536.
[121] M. Vaida, Master Thesis, Freie Universität Berlin, Berlin, 2004.
[122] P.F. Bernath, Spectra of Atoms and Molecules, Oxford University Press, New York, 1995.
[123] R.C. Bell, K.A. Zemski, D.R. Justes, A.W. Castleman Jr., J. Chem. Phys. 114 (2001) 798.